Unravelling multiple thermotectonic events accommodated by the Highland Boundary Fault: Insights from K–Ar dating

Lucy McKay [a,*], Simon J. Kemp [b], Graham A. Leslie [c], Andrew Todd [d], Zoe K. Shipton [e] and Rebecca J. Lunn [f], John Booth [g]

a Department of Civil and Environmental Engineering, James Weir Building, 75 Montrose Street, University of Strathclyde, 75 Montrose Street, Glasgow, U.K., G1 1XJ, lmckay203@gmail.com

Present address: COWI UK, 5th Floor, 310 St Vincent Street, Glasgow, U.K., G2 5RG

[b] British Geological Survey, Environmental Science Centre, Keyworth, Nottingham, NG12 5GG, UK, sjk@bgs.ac.uk

[c] British Geological Survey, The Lyell Centre, Research Avenue South, Edinburgh, EH14 4AP, UK, agle@bgs.ac.uk

[d] CSIRO - Energy, 26 Dick Perry Drive, Kensington, WA 6151, Australia, andrew.todd@csrio.au

[e] Department of Civil and Environmental Engineering, James Weir Building, 75 Montrose Street, University of Strathclyde, 75 Montrose Street, Glasgow, U.K., G1 1XJ, zoe.shipton@strath.ac.uk

[f] Department of Civil and Environmental Engineering, James Weir Building, 75 Montrose Street, University of Strathclyde, 75 Montrose Street, Glasgow, U.K., G1 1XJ, rebecca.lunn@strath.ac.uk

[g] Institute of Earth Sciences - NAWI Graz Geocenter, University of Graz, Universitaetsplatz 2, 8010 Graz, Austria, JBMay16@gmail.com

*Corresponding author: Lucy McKay (lmckay203@gmail.com, +447730027962)

Keywords

Highland Boundary Fault, microstructures, strain, K–Ar dating, clay polytypes, fault reactivation

Abstract

Multiple reactivation episodes and long slip histories lead to complex fault structures, whose unravelling remains challenging in the absence of absolute time constraints. We apply K–Ar isotopic dating of illitic fault rocks, coupled with X-ray diffraction and microstructural analyses to constrain, for the first time, timing of illite-producing brittle fault movements accommodated by the Highland Boundary Fault (HBF), Scotland. Illite Age Analysis (IAA) plots indicate multiple fault reactivation events on the HBF. IAA plots for the red foliated chaotic fault-breccia conform to a 'normal' IAA pattern with younger ages recorded for 'authigenic' 1M illite (306-276 and 300-272 Ma) and older dates for 'detrital' $2M_1$ illite (554-502 and 471-427 Ma). Conversely, IAA plots for the superimposed blue fault-gouge reverse the 'normal' trend, with older 'authigenic' 1M illite (348-314 and 276-25 Ma) and younger 'detrital' $2M_1$ illite (258-234 and 250-226 Ma) ages. We propose this results from heterogeneous shearing and strain localisation. In localised pods of the blue fault-gouge, strain accelerated clay mineral growth, increased crystallite-size, and facilitated polytypic transformation from 1M to $2M_1$ illite via defect migration. Elsewhere in the blue fault-gouge, and in the red foliated chaotic fault-gouge, low strain regimes allowed the 1M polytype to remain unaltered.

1. Introduction

Fault rocks exhumed at the Earth's surface develop through progressive deformation under a range of crustal conditions. A fault core will be the result of multiple, perhaps even tens of thousands of movement events on a single fault, integrated over time and space (McKay et al, 2021). Mechanical and chemical processes can vary through time, occurring at the same time in different parts of the fault system, or at different times in the same part of the fault (e.g., Solum *et al.* 2010). Consequently, the fault core may contain multiple fault rocks, each with different mineralogical and mechanical properties (e.g., clay content and type), thus impacting the frictional behaviour of the fault through time (e.g., Smith and Faulkner, 2010; Tembe *et al.*, 2010; Ikari *et al.*, 2011; Behnsen and Faulkner, 2012; Boulton *et al.*, 2014). The exhumed fault core is complicated by exhumation-related (sometimes syn-tectonic) overprinting as well as the result of multiple integrated events on the fault over time. Multiple reactivations and long slip histories may lead to complex fault structures, the unravelling of which remains challenging in the absence of absolute time constraints. Radiometric dating of authigenic (essentially syn-kinematic) illite in clay-rich fault core rocks, coupled with X-ray diffraction (XRD) and microstructural analysis, offers a unique possibility to decipher fault zone processes, the details of which could otherwise remain hidden in the rock record.

Fault rocks generated in brittle fault cores typically contain crushed rock fragments including metamorphic, magmatic, or detrital sedimentary mica derived from the wallrock, and variable quantities of newly grown authigenic mica (including illite), which may be distinguished from each other by their type of crystallographic stacking, called polytypism

(Verma and Krishna, 1966). In ideal cases, the most widely accepted interpretation is that the $1M/1M_d$ polytype is diagnostic of authigenic illite formed within the brittle fault zone during faulting (essentially syn-kinematic), whereas the $2M_1$ polytype is diagnostic of detrital (old) wallrock material (e.g., Grathoff *et al.*, 2001; Van Der Pluijm *et al.*, 2001; Vrolijk *et al.*, 2018 and references therein). However, it should be noted that none of the many published clay mineral fault-dating studies have provided direct evidence that 1M authigenesis is syn-kinematic; all studies are experimental. Typically, the ratio of $2M_1$ to $1M/1M_d$ polytypes decreases with decreasing grain size (Van Der Pluijm *et al.*, 2001). Experimental studies suggest the $2M_1$ polytype forms at higher temperatures (>280°C) (Velde, 1965; Środon and Eberl, 1984), whereas the $1M/1M_d$ polytype is less stable and forms at lower temperatures (<~200°C) (Velde, 1965; Grathoff *et al.*, 2001). Based on a two end-member mixing model, quantified percentages of each illite polytype ($1M/1M_d$ and $2M_1$) in different clay size fractions, and their apparent K–Ar or ^{40}Ar–^{39}Ar ages, are then used to extrapolate the ages of the 'end-member' wallrock and authigenic illite populations. This methodology is the basis of Illite Age Analysis (IAA, Pevear, 1999). However, assuming that the $2M_1$ polytype is purely of detrital origin may be misleading as authigenic $2M_1$ polytypes have been observed within fault-gouge associated with hydrothermal environments, areas of elevated geothermal gradients, and/or deeper parts of exhumed faults (Zwingmann *et al.*, 2010; Clauer and Liewig, 2013; Viola *et al.*, 2013, 2016; Mancktelow *et al.*, 2015).

Many fault rock studies have successfully dated illitic clay from fault rocks in order to constrain the timing(s) of brittle fault movements in a variety of settings (Van Der Pluijm *et al.*, 2001; Zwingmann and Mancktelow, 2004; Uysal *et al.*, 2006, 2020; Zwingmann *et al.*, 2010; Bense *et al.*, 2013; Viola *et al.*, 2013, 2016; Boles *et al.*, 2015; Mancktelow *et al.*, 2015; Ksienzyk *et al.*, 2016; Ring *et al.*, 2017, 2021; Vrolijk *et al.*, 2018; Aldega *et al.*, 2019; Kemp *et al.*, 2019). K–Ar or ^{40}Ar–^{39}Ar dating of illitic clay from fault rocks has been crucial in understanding the development of convergent plate boundaries and continental collisions (e.g., Van Der Pluijm *et al.*, 2001; Duvall *et al.*, 2011; Isik *et al.*, 2014; Aldega *et al.*, 2019), movement along transform plate boundaries (Uysal *et al.*, 2006; Boles *et al.*, 2015; Ring *et al.*, 2017), and fault reactivation (Viola *et al.*, 2013; Aldega *et al.*, 2019). This study aims to constrain the timing of illite-producing brittle fault movements affecting/superimposed upon an ancient plate boundary fault in Scotland (McKay *et al.*, 2020) – the Highland Boundary Fault (HBF) (**Figure 1**).

The present trace of the HBF coincides with an important terrane-bounding fault in UK geology which has been the subject of many regional tectonic studies (e.g., Bluck, 1985; Dewey and Strachan, 2003; Tanner *et al.* 2007; Tanner, 2008; Cawood *et al.*, 2012). Although the HBF has clearly played an important role in the tectonic evolution of the British Isles (Tanner, 2013a; 2013b; 2013c; 2014; Chew and Strachan, 2014), the fault trace and associated cataclastic fault rocks and fillings are poorly exposed across Scotland and thus its history is poorly constrained. Exposures at Stonehaven, Northeast Scotland, provide a rare opportunity to study the exposed trace of the HBF in detail (**Figure 1**; McKay *et al.* 2020). McKay *et al*. (2020) confirmed that the HBF, in the Stonehaven section at least, records dominant sinistral strike-slip displacement, but also reveals that the fault core consists of lithologically and structurally variable illitic fault rocks (McKay *et al.*, 2020). However, the exact timing of authigenic clay growth and fault movement is unclear from the field evidence alone. In this study, we apply a combination of microstructural analysis, XRD analysis and K–Ar isotopic dating to constrain, for the first time, the timing of illite-producing displacement on the HBF. These results are significant for understanding fault processes and the tectonic evolution of the British Isles and the surrounding regions.

<INSERT FIGURE 1 HERE>

2. Geological Setting: The Highland Boundary Fault

The remarkably straight, present-day trace of the HBF extends NE–SW across Scotland for over 240 km, separating the Scottish Highlands from the Midland Valley of Scotland (**Figure 2a**). The fault is best exposed within a coastal section located ~1 km north of Stonehaven (**Figure 2a,b**). Here, the principal slip surface (PSS) is marked by a relatively straight steep (dip: 66 ± 7°; n = 70), NW-dipping (strike: 059 ± 8°; n = 70) contact that separates carbonate-rich serpentinite rocks and a low grade metabasalt sequence of the Highland Border Ophiolite (to the south-east) from chlorite- to biotite-grade quartzo-feldspathic psammitic and semipelitic metamorphic rocks of the Dalradian Supergroup (to the north-west) (**Figure 2b;** McKay *et al.*, 2020). These rocks are assigned to the Midland Valley and Grampian Highland terranes respectively.

<INSERT FIGURE 2 HERE>

The detailed field mapping of McKay *et al.* (2020) has revealed that the Stonehaven section of the HBF is composed of a structurally and compositionally variable fault core formed during sinistral strike-slip. This fault core consists of four distinct units that remain unmixed: (1) a localised green fault-gouge; (2) a blue fault-gouge of high plasticity (**Figure 2c, d**); (3) a red foliated chaotic fault-breccia where the foliations wrap around cm-scale clasts of wallrock (**Figure 2f**); and, (4) a red crackle fault-breccia with large, elongated wallrock lenses (McKay *et al.*, 2020). Localised pods of the red foliated chaotic fault-breccia are found within the blue fault-gouge at the contact between these two fault fillings suggesting a relative age-relationship of these two units (**Figure 2e, Figure 3**), but overall, the units remain largely unmixed. The highest strain part of the fault core (the PSS) is always at the southern margin.

<INSERT FIGURE 3 HERE>

Across-fault transects perpendicular to the fault plane (structural logs; locations given in **Figure 2b**) reveal that the total thickness of the HBF fault core varies between 2.95–10.7 m over this 560 m along-strike section (McKay *et al.*, 2020). No single unit of the 4 recorded is continuous along strike, and each individual unit varies in thickness. For example, the green fault-gouge is only observed at one location (Log 4) so could either represent a zone of localised alteration, or a remnant fragment of a reworked, previously extensive, fault core lithology. While the fault core varies in thickness, the overall structure of the fault does not change, i.e., localisation within a single fault core strand occurs at all locations along this mapped section of the HBF, and the PSS is always found on the southern edge of the core (**Figure 2g**).

3. Materials and Methods

3.1. Samples

With permission granted by Scottish Natural Heritage (now NatureScot) to sample at this Site of Special Scientific Interest (SSSI), samples were recovered from sections described by three structural logs – Log 4, Log 5, and Log 6. The locations of these samples are indicated by star symbols adjacent to the logs in **Figure 2g**. Samples were limited to those locations exposed by digging through a locally thick layer of beach shingle to uncover the cataclastic fault rocks and the associated clay-rich fillings (gouge), and which were subsequently re-covered with shingle. Orientated sections of the clay were extracted with a shovel tip.

In total, ten thin section mounts were prepared from samples of three different fault core units: green fault-gouge (1 sample), blue fault-gouge (6 samples) and the red foliated chaotic fault-breccia (3 samples). Samples are numbered by the log they were collected from, and the distance along the log from the south-eastern defined limit of the PSS towards the Dalradian rocks in the north-west wall of the fault core (e.g., Log 5-0.3 m). The oriented samples were immediately wrapped in cling film in the field, to minimise drying and shrinking. In the laboratory, the samples were slowly impregnated with epoxy resin to consolidate the soft gouge, preserving delicate structures for microstructural analysis.

3.2. Microstructural Analysis

Thin sections were analysed using a Nikon Eclipse LV100ND petrographic microscope at the University of Strathclyde, with images captured using a Nikon DS-Ri2 5 Megapixel digital camera. Scanned thin section images were imported into ArcGIS and scaled for further analysis. Features such as clasts, strain shadows, fabrics and veins were identified and digitised into different layers within ArcGIS. For polygon features (clasts, veins, and strain shadows), the ArcGIS minimum bounding geometry tool was used to add a layer containing the best fit 'rectangle by width'. This returned the area, perimeter, length, and width of the rectangle (used as a proxy for the long axis and short axis of the feature, the *a* and *b* axis respectively) and the orientation of the long axis. This information was then imported into Microsoft Excel to calculate the aspect ratio, the orientation of the long axis relative to the mean PSS of the HBF as determined from field mapping in McKay *et al.* (2020), and relative circularity of the clasts. As outlined in Mort & Woodcock (2008), circularity was calculated using the formula (equation 1):

$$circularity = 4\pi \left(\frac{area}{perimeter^2}\right) \qquad \text{(eq. 1)}$$

where, a value of 1 represents a perfectly circular shape. The clast size, orientation, aspect ratio and circularity were then compared for the thin sections of different fault core units and from different locations along the fault (Logs 4, 5 and 6). The median value is reported for each property along with the Coefficient of Quartile Variation (CQV), which is a measure of relative dispersion based on the interquartile range. Since CQV is unitless, it is useful for the comparison of variables with different units (i.e., area in cm^2, length of the long axis in cm, aspect ratio and circularity – both of which are unitless). For linear features (e.g., clay fabrics), the orientation was assessed using the 'sets' function of the ArcGIS toolbox Network GT (Nyberg *et al.*, 2018), and calculated relative to the mean orientation of the PSS of the HBF as determined in McKay *et al.* (2020). The orientation of clasts and linear features was only assessed for fully-oriented samples.

3.3. Illite Age Analysis

Following on from the mineralogy presented in McKay *et al.* (2020), two representative samples from each of the blue fault-gouge (Log 4-0.86m and Log 5-0.3m) and red foliated chaotic fault-breccia (Log 4-2.65 m and Log 5-2.7m) were selected for illite age analysis (IAA). These samples were selected as both units are continuous along the Stonehaven section of the fault (**Figure 2**). Samples from Log 4 and Log 5 were dated as these are the locations where the thinnest and widest fault core was recorded (**Figure 2**).

As in similar studies aiming to constrain the timing and origin of fault-gouge at other plate boundary faults (e.g., Boles *et al.*, 2015; Ring *et al.*, 2017; Kemp *et al.*, 2019), the samples were first dispersed in deionised water and different size fractions: 1–0.5 µm (coarse), 0.5–0.2 µm (medium) and <0.2 µm (fine) separated using timed gravity sedimentation and centrifugation. The purpose of this was to attempt to remove any coarse-grained impurities (e.g., quartz, calcite etc.) from the fine-grained clay minerals. Recovered fractions were then oven dried at 105°C prior to analysis.

3.3.1. XRD Analysis

XRD analysis of both oriented samples (used for definitive clay mineral identification) and randomly oriented samples (used for polytype identification and quantification) was conducted at the James Hutton Institute, a UK accredited institute following standard proven methodologies (Omotoso et al, 2006; Butler & Hillier, 2021) For clay mineral identification, small portions of each of the size fractions were dispersed in small volumes of water, then prepared as oriented mounts using the filter peel transfer technique and scanned using

Cobalt Kα radiation from 3–45° 2θ in the air-dried state, after ethylene glycol solvation, and after heating to 300 °C for one hour. The clay minerals identified were quantified using a mineral intensity factor approach based on calculated XRD patterns (Hillier, 2003). Uncertainty is estimated as better than ±5 wt.% at the 95% confidence level.

For polytype analysis, the separated size fractions were gently disaggregated and loaded into sample holders, taking care to avoid preferred orientation and to obtain as random a presentation as possible. XRD scans were recorded from 3–80° 2θ. Due to the complexity of the mineralogical assemblages, polytype analysis was made by a normalised full pattern reference intensity ratio (RIR) method using natural standards for all minerals identified in each size fraction, including $1M_d$ and $2M_1$ illite polytypes.

3.3.2 K–Ar Analysis

K–Ar analysis was performed at CSIRO, Kensington, Australia following the same methodology as that detailed in Kemp *et al.* (2019). During the analysis, two international standards were measured (HD-B1 and LP6) (**Table 1**). The error for Ar analyses was below 0.5% and the $^{40}Ar/^{36}Ar$ value for airshots was 295.74 ± 0.22 Ma (**Table 1**, **Table 2**).

<INSERT TABLE 1 HERE>

<INSERT TABLE 2 HERE>

4. Microstructures: Fault Core Processes Observed Within the Highland Boundary Fault

In this section, key microstructural observations are presented for the blue fault-gouge and red foliated chaotic fault-breccia. The figures show representative thin sections and images from both fault core units.

4.1. Blue Fault-Gouge

The blue fault-gouge consists of sub-rounded to rounded, spherical to elongate clasts embedded in a dark-brown, fine-grained clay-rich gouge matrix. Combining the data from all six samples of the blue fault-gouge, the clasts (n=4895) range in 2D area from 0.06 to 12820.65 cm^2 (median = 1.28 cm^2, CQV = 0.56), the long axis length from 0.31 to 125.95 cm (median = 1.61 cm, CQV = 0.32), the aspect ratio from 1.00 to 8.03 (median = 1.43, CQV = 0,15) and the circularity of 0.20 to 0.94 (median = 0.80, CQV = 0.05).

Some clasts and matrix patches have a preferred orientation producing a fabric (**Figure 4**, **Figure 5**, **Figure 6a**), although the foliation can deflect and wrap around the clasts (**Figure 6b**). For instance, in sample Log 4-0.32m, the clasts and fabric are aligned parallel, ~15° anticlockwise or ~10° clockwise from the PSS of the HBF (**Figure 4a, b**) in Y-, R- or P-shear geometries respectively (**Figure 4c, d**). In sample Log 5-2.25m, the fabric is aligned at high angles (60–75° anticlockwise) from the PSS in R'-shear geometries (**Figure 5c**). Strain shadows are visible at different scales (**Figure 5a, b)**. Strain shadow geometries are σ-type shadows (**Figure 6g**), providing evidence of strain and are aligned in the same direction as the fabric. Parallel, opening-mode veins are also present, aligned at ~55° anticlockwise from the PSS (**Figure 5a, b)** which may represent extensional T-shears. The veins are mineralised with altered, sericitized clay present at the margins.

Typically, the clasts within the blue clay-rich fault-gouge are sub-rounded to rounded (median circularity = 0.80, n = 4895; ***Table 5.2***) so a preferred orientation of the long axis is not always visible (**Figure 5d)**. A few clasts resemble clay-clast aggregates which may be indicative of seismic slip (CCA's; Boutareaud *et al.*, 2008) (**Figure 6c, d**). 'Snowballed' clay rims were observed around rotated, rounded clasts where the fabric swirls around the clast (**Figure 6c**). While some clasts have rounded edges suggestive of mechanical wear, others have tapered, elongate geometries with pressure solution seams along the edges (**Figure 6e**), suggesting a combination of shearing and chemical alteration (Sills *et al.*, 2009). Some clasts display an internal fabric (**Figure 6e**) and/or wings (**Figure 6g**) suggestive of local shearing. Some clasts also have undulated margins (**Figure 6f**) suggestive of melt corrosion/frictional melt. Late-stage veining along a pre-existing fabric is evident in **Figure 6h** and there appears to be a late-stage brittle overprint superimposed upon the ductile shearing features (**Figure 6**).

<INSERT FIGURE 4 HERE>

<INSERT FIGURE 5 HERE>

<INSERT FIGURE 6 HERE>

Surprisingly, marine microfossils are found in sections of the blue fault-gouge (**Figure 7**). These include relatively intact fragments of ancient bryozoans, possibly belonging to the extinct order *Fenestrata*, brachiopods and an echinoid spine (as identified by P.D. Taylor, pers. comm., 2018). Authigenic clay growth must postdate these fossils, which assuming the bryozoans belong to the order *Fenestrata*, are Ordovician to Permian in age. These fossils are sporadically distributed throughout the blue fault-gouge and were only locally observed in one sample (sample Log 4-0.32m) (**Figure 4**). Both primary fabrics and secondary recrystallisation/growth textures are observed within the fossils. However, despite the fossils being preserved within a high-strain fault-gouge, there is no evidence of internal strain (e.g., microfracturing or shear indicators) within the fossil fragments. This suggests strain is not uniform throughout the blue gouge.

<INSERT FIGURE 7 HERE>

4.2. Red Foliated Chaotic Fault-Breccia

The red foliated chaotic fault-breccia consists of sub-rounded to sub-angular, circular to elongate polymineralic clasts embedded in a dark brown to red, fine-grained clay-rich gouge matrix. Individual and aggregated quartz and calcite granules are common. Red, hematitic foliations define a clear structural fabric (**Figure 8a, Figure 9**). The foliations are generally aligned parallel or sub-parallel to the PSS of the HBF but anastomose and wrap around variably altered, poorly sorted (in size not composition), centimetre-scale, metasedimentary clasts of Dalradian wallrock (**Figure 9b, d**). Combining data from all three samples of the red foliated chaotic breccia, the clasts (n=1594) range in 2D area from 0.16 to 5855.12 cm^2 (median = 3.17 cm^2, CQV = 0.7), the long axis length from 0.57 to 99.76 cm (median = 2.85 cm, CQV = 0.5), the aspect ratio from 1.02 to 10.28 (median = 1.72, CQV = 0.3) and the circularity of 0.16 to 0.94 (median = 0.75, CQV = 0.16). The clasts have a preferred alignment displaying a weak fabric (**Figure 9e, f**). For instance, in sample Log6-1m, the long axis of the clasts and aggregates of clasts are aligned parallel or sub-parallel (10–20°) to the PSS of the HBF (**Figure 8a, e**). The clasts do not display tails or strain shadows. Pressure solution seams around the clasts and evidence of dissolution-precipitation is common (e.g., **Figure 9e**). The clasts display an internal fabric, are highly altered, and show evidence of a cross-cutting network of fractures that may be filled with clay (**Figure 9g, h)**. Very few shear fabrics are observed in the red foliated chaotic fault-breccia when compared with the blue fault-gouge material.

<INSERT FIGURE 8 HERE>

<INSERT FIGURE 9 HERE>

5. XRD Mineralogy

XRD analysis reveals that the mineralogical assemblages of the blue fault-gouge and red foliated chaotic fault-breccia are complex, even in the finest size fractions (**Table 3**). Clay minerals identified in the blue fault-gouge include chlorite, kaolinite, interlayered illite/smectite (I/S) and two illite polytypes ($2M_1$ and $1M_d$) (**Table 3, Table 4**). Non-clay minerals identified in the blue fault-gouge include quartz, halite, hematite, rutile and anatase (**Table 3**). Clay minerals identified in the red foliated chaotic fault-breccia include kaolinite, I/S and two illite polytypes ($2M_1$ and $1M_d$) (**Table 3, Table 4**). Unlike the blue fault-gouge, no chlorite was detected in the red foliated chaotic fault-breccia. Non-clay minerals in the red foliated chaotic fault-breccia include quartz, halite, hematite, calcite and anatase (**Table 3**).

Oriented mount XRD suggests that illite and I/S content increases with decreasing size fraction for both blue fault-gouge and red foliated chaotic fault-breccia samples (**Table 4**).

<INSERT TABLE 3 HERE>

<INSERT TABLE 4 HERE>

6. K–Ar Dating of the Highland Boundary Fault

Twelve (plus three duplicates, see section 7.1), covering three size fractions were obtained from the blue fault-gouge and red foliated chaotic fault-breccia (**Table 5**). The K–Ar ages range from 383.4 ± 8.8 Ma (Devonian, Upper Famennian, Log 4-2.65m, 1–0.5µm) to 246.5 ± 5.7 Ma (Triassic, Mid-Anisian, Log 5-0.3m, <0.2µm), with the blue fault-gouge having younger ages compared to the red foliated chaotic fault-breccia. Radiometric ^{40}Ar contents range from 92.7–98.7% indicating reliable analytical conditions for all analyses with no significant radiogenic ^{40}Ar contamination. The K content ranges from 1.75–5.94% with the range reflecting contamination from non-K-bearing mineral phases, which is supported by XRD data (**Table 3, Table 4**). In general, the blue fault-gouge has a lower K-content than the red foliated chaotic fault-breccia because of higher chlorite content. K–Ar ages decrease with decreasing grain size. Duplicate analyses show comparable ages with only a 0.1–0.5% variation.

<INSERT TABLE 5 HERE>

A series of IAA plots were produced using the proportion of the $2M_1$ polytype plotted against the function $\exp^{(\lambda t)-1}$ (where λ is the decay constant of potassium and t is time) with error bars of ±5% applied, similar to the presentation of Kemp *et al.* (2019) (**Figure 10**). It is generally accepted that the K–Ar ages for the finest fraction (<0.2 µm) indicates the timing of the last episode of deformation recorded by fault rock through the growth of synkinematic or authigenic 1M illite (Torgersen *et al.*, 2015; Viola *et al.*, 2016). Whereas the age of the coarsest fraction (1–0.5 µm) can be interpreted as an inherited contribution from the host rock through detrital $2M_1$ illite, under certain conditions, it may indicate an earlier deformation or thermal event (Torgersen *et al.*, 2015; Viola *et al.*, 2016).

The plots for the red foliated chaotic fault-breccia follow the commonly observed trends of decreasing age with decreasing $2M_1$ content i.e., producing younger 'authigenic' 1M and older 'detrital/wallrock' $2M_1$ dates (**Figure 10**). However, the blue fault-gouge samples produce a reverse of the normal trend, with older ages for the 1M illites than the $2M_1$ dates.

<INSERT FIGURE 10 HERE>

7. Discussion

7.1 A record of portioning of polytype behaviour in relation to strain

The IAA plots for the illite-rich assemblages from the red foliated chaotic fault-breccia conform to the 'normal' pattern with younger ages being recorded for 'authigenic' 1M illites (291 and 286 Ma) and older dates for the 'detrital' $2M_1$ illites (528 and 449 Ma). Detrital illites from the wallrock Dalradian Supergroup, perhaps reset by the Caledonian orogeny, offer the most likely explanation for the older dates. A period of fault authigenesis in the Permian corresponds with reactivation noted elsewhere in Scotland (Kemp *et al.*, 2019;

Dichiarante *et al.*, 2016) and recorded dolomitization of serpentinite rock in the HBF footwall damage zone (Elmore *et al.*, 2002). However, the IAA plots for the blue fault-gouge are the reverse of the ‘normal’ trend, with older 'authigenic' 1M illites (331 and 263 Ma) and younger 'detrital' $2M_1$ illites (246 and 238 Ma) ages. How can this reversal be explained, particularly as the temperatures deemed necessary for $2M_1$ illite development should reset the lower temperature 1M illite? A possible explanation might involve the differing fault processes that the red foliated chaotic fault-breccia and the blue fault-gouge have experienced during shearing.

Shear fabrics are well developed in the blue fault-gouge (e.g., **Figure 6)** but were not observed in the red foliated chaotic fault-breccia (**Figure 9**). Strain-related crystal growth is a response to several interactive processes, including mechanical grain rotation of existing minerals, pressure-solution (dissolution) recrystallization and grain boundary migration (dislocation creep) in newly formed minerals (Roberts et al, 1991; Merriman et al, 1995; Kemp & Merriman, 2004; Dellisanti *et al.*,2008). When pelitic rocks are deformed in response to tectonic stress, slaty cleavage develops as a result of interactive mechanical deformation and thermally driven crystallization processes (e.g., Knipe, 1981; Van der Pluijm *et al.*, 1998, Merriman & Frey, 1998). Roberts *et al.* (1991) noted that a significant input of strain energy accelerated clay mineral growth rates in mudrock sequences in North Wales. These authors suggested that increases in effective crystallite size were produced, not only by a strain-induced reduction in the density of dislocations in existing crystals, but also by the simultaneous dissolution and transfer of material from smaller to larger crystallites. As cleavage development intensified, much of this growth was concentrated in P-domains, as previously demonstrated by petrographic transmission electron microscopic (TEM) studies (e.g., Knipe, 1981).

Studies of mudrocks from the Southern Uplands of Scotland, where low-grade metamorphism is closely associated with tectonic fabric development, indicated differences in strain-induced crystal growth and crystallinity between white mica (illite) and chlorite (Merriman *et al.*, 1995). The ability of white mica to store strain energy and recover from subgrain development resulted in more rapid growth to thicker crystallites, atypical of Ostwald ripening. Under similar conditions, chlorite crystals only partially recovered subgrain boundaries leading to smaller crystallite distributions detected by TEM and XRD, compared with those of white mica.

A later study of the role of tectonic strain on illitization in a fault zone in the Northern Apennines, Italy, showed little difference in Kubler Index (KI, the standard index of illite crystallinity) between the deformed rocks within the fault zone and non-deformed rocks outside the fault zone (Dellisanti *et al.*, 2008). However, comparing the structural domains within fault rocks, a systematic increase in illite content and decrease of KI and other crystallinity parameters characterised the scaly cleavage surfaces (shear planes) and the associated deformed (cleavage) domains with respect to the non-deformed lithons. Here the authors suggest that the illitization was isothermal and probably driven by rock deformation that favoured both the dissolution-crystallisation process and enhanced K-rich fluid movement along a network of planar discontinuities (shear planes) and also within the scaly cleavage domains due to their preferentially oriented phyllosilicates. In comparison, illitization was more retarded in the lithon cores, where the more disordered texture of clay particles inhibited fluid passage.

Strain-induced defect migration (dislocation creep), possibly as screw-dislocations (Baronnet, 1992), most likely contributes to the polytypic transformation from $1M_d$ illite to $2M_1$ (Merriman & Peacor, 1998). Further evidence of the effect of tectonic strain on clay mineral growth and development in mudrocks has been evidenced by studies of the synkinematic development of white micas in strain fringes (e.g., Sherlock *et al.*, 2003; Rolland et al, 2008). During compression and cleavage formation, various rigid bodies including graptolites, other fossilised fauna and sulphide minerals may provide adjacent areas of low strain in which white micas can develop via a combination of pressure solution and solution transfer. These strain-fringe micas have provided high-purity synkinematic material that have yielded high precision dates for providing a new approach to dating low-temperature deformation in mudrocks. The crystallinity of the strain-fringe developed micas may therefore differ from those in the wider mudrock matrix produced by inheritance, burial metamorphism and/or previous metamorphic events.

We therefore propose that the 'late-stage' shearing recorded in the blue fault-gouge was responsible for the synkinematic development of $2M_1$ illites at the expense of earlier formed 1M polytypes. This recrystallisation must have led to resetting of the K–Ar systematics and the younger ages produced. The post-shearing development of $2M_1$ illites and recovery from a strain-related reduction in crystallite size also suggests deep burial of the original shear zone (Merriman & Frey, 1998). Shearing and strain were clearly not uniform throughout the blue gouge, resulting in pods of recrystallised $2M_1$ illite and other areas where little or no recrystallisation occurred. The lack of deformation shown by fossils corroborates this heterogeneity in the blue gouge, although they do show recrystallisation textures. Low strain maintains the 1M polytype, whereas $2M_1$ authigenesis may develop where strain rates increase. Within the blue gouge, the 1M polytype is therefore related to low strain zones (i.e., the localised sections where Ordovician–Permian marine microfossils are preserved, **Figure 7**) whereas the $2M_1$ polytype developed in the higher strain zones.

These new findings imply that the stability of different illite polytypes in fault zones are not just dependent on temperature (i.e., thermodynamics) but also on kinematic factors such as strain, composition, fluid oversaturation etc.

7.2 Geological Interpretation

The IAA dates acquired in this study indicate multiple fault reactivation episodes in a record of prolonged fault activity accommodated by the HBF through the Palaeozoic and into the Mesozoic (**Figure 11**). A geological interpretation of the new IAA data is set out below.

<INSERT FIGURE 9 HERE>

7.2.1 Cambrian Event – Inherited Protolith

The 554-502 Ma $2M_1$ age range from the red foliated chaotic fault-breccia (sample Log5-2.7m) may be interpreted as reflecting the formation age, or partial resetting of, detrital illite derived from Dalradian Supergroup sediments supplied from wall rocks via grain size reduction and plucking. The HBF fault core at Stonehaven exhibits the process of grain size reduction *in situ,* spanning nearly the full range of stages of each filling (McKay *et al.*, 2020). Within the Dalradian, the metagreywacke beds, which locally contain quartz granules, are mechanically stronger and more coherent than interbedded micaceous pelites. For instance, after plucking, these metagreywackes could account for the majority of clasts in the fault core clays. Individual and aggregated quartz and calcite granules are common in the red foliated chaotic fault-breccia (**Figure 9**), possibly sourced from competent protoliths (e.g., sedimentary granule conglomerates/ metagreywackes) in the Dalradian. The mechanically weaker pelitic beds would disaggregate at the grain-scale forming the clay-rich matrix to the red foliated chaotic fault-breccia. The red foliated chaotic fault-breccia could therefore have been derived from the Dalradian wallrock through plucking and abrasion and altered through later faulting events (e.g., Faulting event 4).

7.2.2 Ordovician Event – Inherited Protolith

The 471-427 Ma $2M_1$ age range from the red foliated chaotic fault-breccia (sample Log4-2.65m) overlaps with U-Pb ages (*c*. 453 Ma) derived for magmatic zircons from the Midland Valley (Badenszki *et al.* 2019). Based on their isotopic composition, these magmatic zircons are interpreted to be derived from a buried Late Ordovician magmatic arc situated within the Midland Valley (Badenszki *et al.* 2019), and which developed after the early Ordovician (Tremadoc) arc accretion-related deformation events associated with the *c*. 470 Ma Grampian Events of the Caledonian Orogeny. The 471-427 Ma date also broadly coincides with Lu–Hf and Sm–Nd ages (c. 450 Ma) obtained from prograde garnets within the Moine Nappe of the Northern Highland terrane, associated with a Late Ordovician regional metamorphic event (Bird *et al*. 2013). There were multiple accretion events during the Caledonian Orogeny (Bird *et al*. 2013). Therefore, the 471-427 Ma age range may be connected to development of this Late Ordovician magmatic arc and its related fluids following on after the end of Grampian metamorphism and deformation. The 471-427 Ma age range may indicate the resetting of detrital illite initially derived from the comminution of Dalradian Supergroup wallrock. Movements and heating during the Caledonian orogeny (490–430 Ma) would seem feasible mechanisms for such resetting.

7.2.3 Carboniferous Faulting – Faulting Event 1

The 348-314 Ma 1M age range from the blue fault-gouge (Log4-0.86m) corresponds with the waning stages of the Strathclyde Group deposition and eruption/emplacement of the Clyde Plateau/Bathgate Hills volcanic formations, prior to the deposition of the carbonate-rich succession of the Clackmannan Group. This period of the Visean was accompanied by considerable basin geometry adjustment (Stephenson *et al*. 2003; Monaghan *et al*., 2014). The development of 1M illite may therefore reflect increased basin fault and enhanced volcanic fluid movement and associated alteration, driven by the increased volcanic activity.

Movements on the HBF during the Devonian and Lower Carboniferous have been regarded as essentially mainly normal in style, with downthrow to the south-east into the Midland Valley graben (Cameron and Stephenson, 1985; Paterson *et al.*, 1990) but see also Underhill et al. (2008) who argue for dextral-oblique slip at this time. East–west-trending late Carboniferous quartz-dolerite dykes, observed at intervals throughout the Highland Boundary fault zone, apparently cross the fault zone without displacement, indicating that significant lateral movement had effectively ceased by ~300 Ma (Anderson, 1947; George, 1960).

Particularly noteworthy is the presence of well-preserved fragments of presumably Ordovician–Permian marine fossils within the blue fault-gouge. Irrespective of the mode of movement on the HBF during this period, their presence implies that strain is not uniform within the blue fault-gouge. The well-preserved fossil fragments show no evidence of internal strain (**Figure 7**) despite being caught up in the sinistral shearing recorded by the surrounding higher strain blue clay-rich fault gouge.

7.2.4 Permian Faulting – Faulting Event 2

The 306–250 Ma age ranges recorded by 1M illites from both the red foliated chaotic fault-breccia samples (Log4-2.65m and Log5-2.7m) and one of the blue fault-gouge samples (Log5-0.3m) are consistent with those produced by $2M_1$ illite from the Sronlairig Fault (Kemp *et al.*, 2019) and dates for Permian-reactivated Devonian structures in the Pentland Firth coast section (Dichiarante *et al.*, 2016).

Elmore *et al.* (2002) suggest the dolomitization of serpentinite rock in the HBO at Stonehaven occurred in the late Permian at *c*. 260 Ma – suggesting that the HBF was a conduit for fluids at this time resulting in dolomitization, silicification and hematite authigenesis. Fluid inclusion and geochemical studies indicate that the fluids were hydrothermal in origin (110-240°C) and had a range of sources associated with high levels of crustal heat flow due to igneous activity in the Carboniferous-Permian (Elmore *et al.*, 2002).

1M illite authigenesis may represent the lower temperature, waning phase of this alteration episode. The origin of the fluids could be related to the intrusion of late Carboniferous to early Permian dykes in central Scotland (Stephenson *et al*., 2003), and suggests reactivation of the HBF in the Carboniferous–Permian accommodating fluid movement.

7.2.5 Triassic Faulting – Faulting Event 3

The 258 to 226 Ma age range presented by the $2M_1$ illites (see section 7.1) from the blue fault-gouge (Log5-0.3m and Log4-0.86m) are younger than any previously reported for the onshore UK. Similar ages have however been reported from the Norwegian sector of the North Sea rift shoulder, particularly in the Viking Graben (Fossen *et al*., 2021). The northern North Sea rift basin formed during a two-phase rift history well-documented form extensive hydrocarbon exploration. K-Ar ages recorded in fault gouge from the North Sea indicate fault activity between 270Ma – 230 Ma (Rift Phase 1) and 170Ma – 135 Ma (Rift Phase 2) (Fossen *et al*., 2021). The earlier phase, which the HBF seems to correspond to, saw rift basins initiated in the Permian with an Early Triassic climax (Færseth, 1996; Roberts et al., 1995). Mid-Permian extension resulting in the Northern Atlantic and North Sea rift systems propagated southwards from East Greenland to initiate fracturing of the Viking (and Central) grabens of the North Sea basin, along with fault-block rotation in the East Shetland Basin (Glennie, 2000).

There are multiple seismically mappable unconformities in the Olenkian to Anisian/Ladinian part of the early Triassic e.g., a major intra-Triassic unconformity, which has long been correlated with, and named after, the Hardegsen Unconformity of the German Basin

(Newall, 2018). The Hardegsen Unconformity (alternatively known as the 'Mid-Triassic' unconformity as it may not be an exact correlation), is widespread stretching across the Cheshire Basin, Wessex Basin, Worcester Graben, East Irish Sea Basin and East Midlands (Newall, 2018). The unconformity is typically referred to as an Olenikian event so nominally older than our dated movements on the HBF but clearly there is regional-scale disturbance around 240 Ma where the North Sea basin is stretching/forming from about this time onwards (Fossen et al. 2021), along with the beginnings of widespread marine incursion into the Triassic mudstone groups (Mercia etc.). Furthermore, the Great Glen Fault is reported to have undergone minor normal adjustments in the Permo-Triassic and limited dextral shift during late Triassic–early Cretaceous times (McQuillin *et al.*, 1982; Allen, 2019 and references therein). The new K–Ar dates reported in this study argue that the HBF accommodated significant left-lateral movement, contemporaneous with this episode of E–W-oriented extension and rifting. As such, the HBF would have been ideally oriented to act as a (sinistral) P-shear in this early Mesozoic stress regime. It is possible that the HBF was acting to accommodate developing hard linkage between the Northern and Central North Sea rifts and the Irish Sea basins, and perhaps further west still (*cf*. Fig.10.2, Glennie, 2000).

Note that none of these new results show evidence of late Jurassic/early Cretaceous fault activity and related mineral growth as is now known to have occurred around the Great Glen Fault and the Moray Firth region (Kemp et al. 2019; Tamas et al., 2022, 2023), perhaps suggesting that such younger Mesozoic tectonism was more prevalent to the north-west of the Highland Boundary Fault damage zone.

The K–Ar ages presented here are consistent with the field observations of the blue fault-gouge containing localised pods of the red foliated chaotic fault-breccia (**Figure 3**). The localised red pods at the contact between the blue fault-gouge and red foliated chaotic fault-breccia (**Figure 3**) may represent ripout clasts similar to those described for other strike-slip faults (Swanson 1989, 2005; DiToro & Pennacchioni 2005). For instance, when the fault became locked, or there was a reason for widening, the fault plucked out bits of the sidewall forming ripout clasts adjacent to the leading slip plane. The ripout clasts were initially displaced into the fault core through dilation and cementation, resulting in the incorporation of altered sidewall maternal (i.e., altered red foliated chaotic fault-breccia) into the blue fault-gouge with geometries consistent with the sinistral sense of shear of the bounding faults. The red pods, bleached clasts and white altered foliation are all aligned in Y-, P- or R-shear Reidel geometries (**Figure 3**) suggesting that small-scale, antithetic and synthetic shears, and associated fluid flow along these shears, appears to 'mix' the zone i.e., the units are not chemically mixed. As observed for other faults, the formation of these ripout clasts are a function of fault roughness – they represent asperities that were sheared off from a rough surface (e.g., Shervais & Kirkpatrick 2016). The formation of these red pods (i.e. ripout clasts) may explain the heterogeneity in fault core thickness observed over a short distance along the fault length (McKay *et al.* 2020). The fact that the red pods are found in the blue gouge, and not the other way around, suggests the red cataclasite is older than the blue gouge, conforming to the K–Ar ages presented in this study.

7.3 Implications for localised reactivation of fault gouges in other large clay-rich faults

A total age span of 296-276 Ma separates the oldest and the youngest fractions in the clay-rich fault rocks of the HBF (**Figure 11**), which is remarkable considering that all twelve fractions are from the same fault core. The dates are not random but are consistent with structural and textural constraints and define a clear correlation with grain size. IAA plots for the red foliated chaotic fault-breccia conform to the 'normal' pattern of positively correlated K-Ar ages with grain size (the ratio of $2M_1$ to $1M/1M_d$ polytypes decreases with decreasing grain size). Conversely, IAA plots for the superimposed blue fault-gouge reverse the 'normal' trend (the ratio of $2M_1$ to $1M/1M_d$ polytypes increases with decreasing grain size) (**Figure 10**).

In this paper we suggest that this reversal in IAA trends is the result of the differing fault processes that the red foliated chaotic fault-breccia and the blue fault-gouge have experienced during shearing and localised strain. Shearing and strain were clearly not uniform throughout the blue gouge, resulting in pods of recrystallised $2M_1$ illite and other areas where little or no recrystallisation occurred. The lack of deformation shown by marine microfossils (**Figure 7**) corroborates this heterogeneity in the blue gouge, although they do show recrystallisation textures. In certain localised pods of the blue fault-gouge localised strain accelerated clay mineral growth, increased crystallite-size, and facilitated polytypic transformation from 1M to $2M_1$ illite via defect migration. Elsewhere in the blue fault-gouge, and in the red foliated chaotic fault-gouge, low strain regimes allowed the 1M polytype to remain unaltered. Within the blue gouge, the 1M polytype is therefore related to low strain zones (i.e., the localised sections where Carboniferous–Permian marine microfossils are preserved, **Figure 7**) whereas the $2M_1$ polytype developed in the higher strain zones.

The results of this study provide evidence for the temporal evolution of strain localisation on a large offset clay-rich fault. Fault and microstructural observations also demonstrate the strain localisation is not only temporally variable but also spatially variable with along strike variability in terms of thickness, structure and composition evident over different length scales (McKay et al., 2020). Detailed microstructural analysis accompanying IAA of illite-rich fault rocks may find that such temporally and spatially variable, localised reactivation of fault gouges is common in similar large offset clay-rich faults.

8. Conclusions

Although the HBF has played an important role in the tectonic evolution of the British Isles, the fault trace and associated cataclastic fault rocks and fillings are poorly exposed across Scotland and thus its movement history has been poorly constrained. Exposures at Stonehaven, NE Scotland, provide a rare opportunity to study the exposed trace of the HBF in detail and interrogate regionally important tectonic frameworks.

By combining XRD and microstructural analysis with polytype identification and quantification, IAA of illite-rich fault rocks has revealed, for the first time, multiple thermotectonic events accommodated by the HBF. The IAA plots for the illite-rich assemblages from the red foliated chaotic fault-breccia conform to the ‘normal’ pattern with younger ages being recorded for ‘authigenic’ 1M illites (306-276 and 300-272 Ma) and older dates for the ‘detrital’ $2M_1$ illites (554-502 and 471-427 Ma). Detrital illites from the wallrock Dalradian Supergroup, perhaps reset by the Caledonian orogeny, offer the most simplistic explanation for the older dates. A period of fault authigenesis in the Permian corresponds with reactivation noted elsewhere in Scotland and recorded dolomitization of serpentinite rock in the HBF footwall damage zone. However, the IAA plots for the blue fault-gouge are the reverse of the ‘normal’ trend, with older 'authigenic' 1M illites (348-314 and 276-250 Ma) and younger 'detrital' $2M_1$ illites (258-234 and 250-226 Ma) ages. Shear fabrics are well developed in the blue fault-gouge but were not observed in the red foliated chaotic fault-breccia. Therefore, as evident by the microstructural observations, we propose this reversal is due to differing shearing regimes that the red foliated chaotic fault-breccia and the blue fault-gouge have experienced. These results imply that the stability of different illite polytypes in fault zones are not just dependent on temperature (i.e., thermodynamics) but also on kinematic factors such as strain, composition, fluid oversaturation etc. Detailed microstructural analysis accompanying IAA of illite-rich fault rocks may find that such localised reactivation of fault gouges is common in similar large offset clay-rich faults.

These new findings imply that the HBF, probably acting as a P-shear within early Triassic E–W-oriented extension, accommodated previously unknown and significant strain contemporaneous with early development of the North Sea and Irish Sea rift basins.

Acknowledgements

We thank Scottish Natural Heritage (now NatureScot), and associated landowners for permission to sample at this Site of Special Scientific Interest. We also thank Spectrum

Petrographics for creating the thin sections and the James Hutton Institute for providing detailed XRD analysis. SJK and AGL publish with the permission of the Executive Director, British Geological Survey (UKRI).

Funding

This work was funded by an Engineering and Physical Science Research Centre (EPSRC) Doctoral Training Partnership (DTP) award (award reference 1904102), a Geological Society of London Research Grant from the William George Fearnsides fund, National Capability funding through the UK Structure project within BGS, and from a generous donation by John Booth.

References

Aldega, L., Viola, G., Casas-Sainz, A., Marcén, M., Román-Berdiel, T. & van der Lelij, R., 2019. Unraveling Multiple Thermotectonic Events Accommodated by Crustal-Scale Faults in Northern Iberia, Spain: Insights From K–Ar Dating of Clay Gouges. *Tectonics,* 38, 3629–3651. https://doi.org/10.1029/2019TC005585

Allen, M., 2019. The long and moving story of the Great Glen Fault. *Mercian Geologist*, 19, 4.

Anderson, J.G.C. 1947. The geology of the Highland Border: Stonehaven to Arran. *Transactions of the Royal Society of Edinburgh*, 61, 479-515. https://doi.org/10.1017/S008045680000483X

Badenszki, E., Daly, J.S., Whitehouse, M.J., Kronz, A., Upton, B.J.G. & Horstwood, M.S.A., 2019. Age and Origin of Deep Crustal Mega-igneous Xenoliths from the Scottish Midland Valley: Vestiges of an Early Palaeozoic Arc and 'Newer Granite' Magmatism. *Journal of Petrology*, 60, 8, 1543-1574. https://doi.org/10.1093/petrology/egz039

Baronnet, A., 1992. Polytypism and stacking disorder. In: Minerals and Reactions at the Atomic Scale: Transmission Electron Microscopy (ed. P. R. Buseck), *Mineralogical Society of America Reviews in Mineralogy*, 27, 231– 288.

Behnsen, J. & Faulkner, D.R., 2012. The effect of mineralogy and effective normal stress on frictional strength of sheet silicates. *Journal of Structural Geology*, 42, 49–61. https://doi.org/10.1016/j.jsg.2012.06.015

Bense, F., Wemmer, K., Lobens, S. & Siegesmund, S., 2013. Fault-gouge analyses: K–Ar illite dating, clay mineralogy and tectonic significance—a study from the Sierras Pampeanas, Argentina. *International Journal of Earth Sciences,* 103, 189–218. https://doi.org/10.1007/s00531-013-0956-7

Bluck, B.J., 1985. The Scottish paratectonic Caledonides. *Scottish Journal of Geology,* 21, 437–464. https://doi.org/10.1144/sjg21040437

Boles, A., van der Pluijm, B.A., Mulch, A., Mutlu, H., Uysal, I.T. & Warr, L.N., 2015. Hydrogen and 40Ar/39Ar isotope evidence for multiple and protracted paleofluid flow events within the long-lived North Anatolian Keirogen (Turkey). *Geochemistry, Geophysics, Geosystems*, 16, 1975–1987. https://doi.org/10.1002/2015GC005810.

Boulton, C., Moore, D.E., Lockner, D.A., Toy, V.G., Townend, J. & Sutherland, R., 2014.

Frictional properties of exhumed fault-gouges in DFDP-1 cores, Alpine Fault, New Zealand. *Geophysical Research Letters*, 41, 356–362. https://doi.org/10.1002/2013GL058236

Boutareaud, S., Calugaru, D.G., Han, R., Fabbri, O., Mizoguchi, K., Tsutsumi, A. & Shimamoto, T., 2008. Clay-clast aggregates: A new textural evidence for seismic fault sliding? *Geophysical Research Letters,* 35, 1–5. https://doi.org/10.1029/2007GL032554

Butler, B.M.& Hillier, S. 2021. Automated Full-Pattern Summation of X-Ray Powder Diffraction Data For High-Throughput Quantification of Clay-bearing minerals. Clay and Clay Minerals, 69, 38-51. https://doi.org/10.1007/s42860-020-00105-6

Cameron, I.B. & Stephenson, D., 1985. *British Regional Geology: The Midland Valley of Scotland* (3rd edition). HMSO, London for the British Geological Survey.

Cawood, P.A., Merle, R.E., Strachan, R.A. & Tanner, P.W.G., 2012. Provenance of the Highland Border Complex: constraints on Laurentian margin accretion in the Scottish Caledonides. *Journal of the Geological Society London*, 169, 575–586. https://doi.org/10.1144/0016-76492011-076

Chew, D.M. & Strachan, R.A., 2014. The Laurentian Caledonides of Scotland and Ireland. In: Corfu, F., Gasser, D., Chew, D.M. (Eds.), New Perspectives on the Caledonides of Scandinavia and Related Areas. *Geological Society London, Special Publications*, 390, 45–91. https://doi.org/10.1144/SP390.16

Clauer, N. & Liewig, N., 2013. Episodic and simultaneous illitization in oil-bearing brent group and fulmar formation sandstones from the northern and southern north sea based on illite K–Ar dating. *AAPG Bulletin*, 97, 2149–2171. https://doi.org/10.1306/04021312122

Dellisanti, F., Pini, G. A., Tateo, F. & Baudin, F. 2008. The role of tectonic shear strain on the illitization mechanism of mixed-layers illite–smectite. A case study from a fault zone in the Northern Apennines, Italy. *International Journal of Earth Science*, 97, 601–616. https://doi.org/10.1007/s00531-007-0180-4

Dewey, J.F. & Strachan, R.A., 2003. Changing Silurian − Devonian relative plate motion in the Caledonides : sinistral transpression to sinistral transtension. *Journal of the Geological Society London*, 160, 219–229. https://doi.org/10.1144/0016-764902-085

Dichiarante, A.M., Holdsworth, R.E., Dempsey, E.D., Selby, D., McCaffrey, K.J.W., Michie, U.McL., Morgan, G. & Bonniface, J. 2016. New structural and Re–Os geochronological evidence constraining the age of faulting and associated mineralisation in the Devonian Orcadian Basin, Scotland. *Journal of the Geological Society*, 173, 457-473. https://doi.org/10.1144/jgs2015-11

Duvall, A.R., Clark, M.K., van der Pluijm, B.A. & Li, C., 2011. Direct dating of Eocene reverse faulting in northeastern Tibet using Ar-dating of fault clays and low-temperature thermochronometry. *Earth and Planetary Science Letters*, 304, 520–526. https://doi.org/10.1016/j.epsl.2011.02.028

Elmore, R.D., Parnell, J., Engel, M.H., Baron, M., Woods, S., Abraham, M. & Davidson, M., 2002. Palaeomagnetic dating of fluid-flow events in dolomitized rocks along the Highland Boundary Fault, central Scotland. *Geofluids*, 2, 299–314. https://doi.org/10.1046/j.1468-8123.2002.00045.x

Færseth, R.B., 1996. Interaction of Permo-Triassic and Jurassic extensional fault-blocks during the development of the northern North Sea. *Journal of the Geological Society*, 153 (6), 931. https://doi.org/10.1144/gsjgs.153.6.0931

Faulkner, D.R., Jackson, C.A.L., Lunn, R.J., Schlische, R.W., Shipton, Z.K., Wibberley, C.A.J., & Withjack, M.O., 2010. A review of recent developments concerning the structure, mechanics and fluid flow properties of fault zones. *Journal of Structural Geology*, 32, 1557–1575. https://doi.org/10.1016/j.jsg.2010.06.009

Fossen, H., Ksienzyk, A.K., Rotevatn, A., Bauck, M.S. and Wemmer, K., 2021. From widespread faulting to localised rifting: Evidence from K-Ar fault gouge dates from the Norwegian North Sea rift shoulder. *Basin Research*, **33**, 1934–1953.

George, T. N., 1960. The stratigraphical evolution of the Midland Valley. *Transactions Geological Society Glasgow*, 24, 32–107

Glennie, K.W. 2000. Permian and Triassic. In: Trewin N. H. (ed.). *The Geology of Scotland*, 4th edition. The Geological Society, London, 301–322.

Gradstein, F., Ogg, J. & Smith, A., 2004. *A Geologic Time Scale 2004.* Cambridge University Press: Cambridge. https://doi.org/10.1017/CBO9780511536045

Grathoff, G.H., Moore, D.M., Hay, R.L. & Wmmer, K., 2001. Origin of illite in the Lower Paleozoic of the Illinois Basin: evidence for brine migration. *Geological Society of America Bulletin*, 113, 1092–1104. https://doi.org/10.1130/0016-

7606(2001)113%3C1092:OOIITL%3E2.0.CO;2

Hess, J.C. & Lippolt, H.J., 1994. Compilation of K–Ar measurements on HD-B1 standard biotite. In: Odin, G.S. (Ed.), *Phanerozoic Time Scale*. Bulletin de Liaison et d'information, IUGS Subcommission, Geochronology, Paris, France, 19–23.

Hillier, S., 2003. Quantitative analysis of clay and other minerals in sandstones by X-ray powder diffraction (XRPD). In: RH, W., S, M. (Eds.), *Clay Minerals in Sandstones.* Association of Sedimentologists Special Publication 34, 213–251.

Ikari, M.J., Niemeijer, A.R. &Marone, C., 2011. The role of fault zone fabric and lithification state on frictional strength, constitutive behavior, and deformation microstructure. *Journal of Geophysical Research*, 116, 1–25. https://doi.org/10.1029/2011JB008264

Isik, V., Uysal, I.T., Caglayan, A. & Seyitoglu, G., 2014. The evolution of intraplate fault systems in central Turkey: Structural evidence and Ar-Ar and Rb-Sr age constraints for the Savcili Fault Zone. *Tectonics,* 33, 1875–1899. https://doi.org/10.1002/2014TC003565

Kemp, S.J. & Merriman, R.J. 2004. Metamorphism of Lower Palaeozoic rocks from the Moffat district, southern Scotland, 1:50KSheet 16W. British Geological Survey Internal Report, IR/04/120. 21pp.

Kemp, S.J., Gillespie, M.R., Leslie, G.A., Zwingmann, H. & Campbell, S.D.G., 2019. Clay mineral dating of displacement on the Sronlairig Fault: implications for Mesozoic and Cenozoic tectonic evolution in northern Scotland. *Clay Minerals*, 54, 181–196. https://doi.org/10.1180/clm.2019.25

Knipe, R.J. 1981. The interaction of metamorphism and deformation in slates. Tectonophysics, 78, 249-72. https://doi.org/10.1016/0040-1951(81)90016-0

Ksienzyk, A.K., Wemmer, K., Jacobs, J., Fossen, H., Schomberg, A.C., Süssenberger, A., Lünsdorf, N.K. & Bastesen, E., 2016. Post-caledonian brittle deformation in the Bergen area, West Norway: Results from K–Ar illite fault-gouge dating. *Norwegian Journal of Geology,* 96, 275–299. https://doi.org/10.17850/njg96-3-06

Mancktelow, N., Zwingmann, H., Campani, M., Fügenschuh, B. & Mulch, A., 2015. Timing and conditions of brittle faulting on the Silltal-Brenner Fault Zone, Eastern Alps (Austria). *Swiss Journal of Geosciences*, 108, 305–326. https://doi.org/10.1007/s00015-015-0179-y

McKay, L., Shipton, Z.K., Lunn, R.J., Andrews, B., Raub, T.D. & Boyce, A.J., 2020. Detailed internal structure and along-strike variability of the core of a plate boundary fault: The highland boundary fault, Scotland. *Journal of the Geological Society*, 177, 283–296. https://doi.org/10.1144/jgs2018-226

McKay L., Lunn R. J., Shipton Z. K., Pytharouli S., &Roberts J. J. 2021. Do intraplate and plate boundary fault systems evolve in a similar way with repeated sip events? *Earth and Planetary Science Letters*. 559, 116757. https://doi.org/10.1016/j.epsl.2021.116757

McQuillin, R., Donato, J.A. & Tulstrup, J., 1982. Development of basins in the Inner Moray Firth and the North Sea by crustal extension and dextral displacement of the Great Glen Fault. *Earth and Planetary Science Letters*, 60, 1, 127–139. https://doi.org/10.1016/0012-821X(82)90028-0

Merriman, R.J. & Frey, M., 1998. Patterns of very low-grade metamorphism in metapelitic rocks. In: Frey M, Robinson D (eds) Low-grade metamorphism. Blackwell, Glasgow, pp 61–107. https://doi.org/10.1002/9781444313345.ch3

Merriman, R.J. & Peacor, D.R., 1998. Very low-grade metapelites: mineralogy, microfabrics and measuring reaction progress. In: Frey M, Robinson D (eds) Low-grade metamorphism. Blackwell, Glasgow, pp 10–60. https://doi.org/10.1002/9781444313345.ch2

Merriman, R.J., Roberts, B., Peacor, D.R. & Hirons S.R., 1995. Strain-related differences in the crystal growth of white mica and chlorite: a TEM and XRD study of the development of metapelitic microfabrics in the Southern Uplands thrust terrane, Scotland. *Journal of Metamorphic Geology*, 13, 559–576. https://doi.org/10.1111/j.1525-1314.1995.tb00243.x

Monaghan, A.A., Browne, M.A.E. and Barford, D.N. 2014. An improved chronology for the Arthur's Seat volcano and Carboniferous magmatism of the Midland Valley of Scotland. *Scottish Journal of Geology*, 50, 165-172.

Mort, K. & Woodcock, N.H., 2008. Quantifying fault breccia geometry: Dent Fault, NW England. *Journal of Structural Geology*, 30, 701–709. https://doi.org/10.1016/j.jsg.2008.02.005

Nyberg, B., Nixon, C.W., & Sanderson, D.J., 2018. NetworkGT: A GIS tool for geometric and topological analysis of two-dimensional fracture networks. *Geosphere*, 14, 1618–1634.

https://doi.org/10.1130/GES01595.1

Odin, G., et al, 1982. Interlaboratory standards for dating purposes. In: Odin, G.S. (Ed.), *Numerical Dating in Stratigraphy*. John Wiley and Sons: Chichester, 123–148.

Omotoso, O., McCarty, D.K., Hillier, S., Kleeberg, R. 2006. Some successful approaches to quantitative mineral analysis as revealed by the 3rd Reynolds Cup Contest. Clays and Clay Minerals, Vol. 54, No. 6, 748–760. https://doi.org/10.1346/CCMN.2006.0540609

Paterson, I.B., Hall, I.H.S. & Stephenson, D., 1990. Geology of the Greenock district. *Memoir of the British Geological Survey*, Sheet 30W and part of Sheet 29E (Scotland).

Pevear, D.R., 1999. Illite and hydrocarbon exploration. Proceedings of the National Academy of Sciences of the United States of America 96, 3440–3446. https://doi.org/10.1073/pnas.96.7.3440

Ring, U., Tonguc Uysal, I., Glodny, J., Cox, S.C., Little, T., Thomson, S.N., Stübner, K. & Bozkaya, Ö., 2017. Fault-gouge dating in the Southern Alps, New Zealand. *Tectonophysics*, 717, 321–338. https://doi.org/10.1016/j.tecto.2017.08.007

Ring, U., Uysal, I.T., Tong, K. & Todd, A., 2021. K–Ar fault-gouge dating in the Lower Buller gorge constrains the formation of the Paparoa Trough, West Coast, New Zealand. *New Zealand Journal of Geology and Geophysics*, 64, 49–61. https://doi.org/10.1080/00288306.2020.1808025

Roberts, B., Merriman, R. J. & Pratt, W., 1991. The influence of strain, lithology and stratigraphical depth on white mica (illite) crystallinity in mudrocks from the vicinity of the Corris Slate Belt, Wales: implications for the timing of metamorphism in the Welsh Basin. *Geological Magazine*, 128, 633– 645. https://doi.org/10.1017/S0016756800019737

Roberts, A.M., Yielding G.; Kusznir N.J., Walker, I.M., & Dorn-Lopex, D., 1995. Quantitative analysis of Triassic extension in the northern Viking Graben. *Journal of the Geological Society,* 152 (1), 15-26. https://doi.org/10.1144/gsjgs.152.1.0015

Rolland, Y., Rossi, M., Cox, S.F., Corsini, M., Mancktelow, N.,Pennacchioni, G., Fornari, M. & Boullier, A.M., 2008. 40Ar/39Ar dating of synkinematic white mica: insights from fluid-rock reaction in low-grade shear zones (Mont Blanc Massif) and constraints on timing of deformation in the NW external Alps. *Geological Society, London, Special Publication*, 299. https://doi.org/10.1144/SP299.18

Sherlock, S.C., Kelly, S.P., Zalasiewicz, J.A., Schofield, D.I., Evans, J.A., Merriman, R.J. & Kemp, S.J. 2003. Precise dating of low-temperature deformation: Strain-fringe analysis by 40Ar-39Ar laser microprobe. *Geology*, 31(3), 219–222. https://doi.org/10.1130/0091-7613(2003)031%3C0219:PDOLTD%3E2.0.CO;2

Sills, D., Chester, J.S. & Chester, F.M., 2009. Shape Preferred Orientation of Porphyroclasts in the Active Gouge Zones of the San Andreas Fault at SAFOD. *EOS Transactions American Geophysical Union*, 90, 52, Fall Meeting Supplement, Abstract #T43A-2057.

Smith, S.A.F. & Faulkner, D.R., 2010. Laboratory measurements of the frictional properties of the Zuccale low-angle normal fault, Elba Island, Italy. *Journal of Geophysical Research*, 115, 1–17. https://doi.org/10.1029/2008JB006274

Solum, J.G., Davatzes, N.C. & Lockner, D.A., 2010. Fault-related clay authigenesis along the Moab Fault: Implications for calculations of fault rock composition and mechanical and hydrologic fault zone properties. *Journal of Structural Geology*, 32, 1899–1911. https://doi.org/10.1016/j.jsg.2010.07.009

Srodon, J. & Eberl, D.D., 1984. Illite. In: Bailey, W. (Ed.), *Reviews in Mineralogy.* Mineralogical Society of America, 495–555.

Stephenson, D., Loughlin, S.C., Millward, D., Waters, C.N. and Williamson, I.T. 2003. Carboniferous and Permian igneous rocks of Great Britain north of the Variscan front. Geological Conservation Review Series, No 27, Joint Nature Conservation Committee, Peterborough. 374 pp.

Tamas, A., Holdsworth, R.E., Tamas, D.M., E. D. Dempsey, E.D., Hardman, K., Bird, A., Roberts, N.M.V., Lee, J., Underhill, J. R., McCarthy, D., , McCaffrey, K.J.W., & Selby, D., 2023. Older than you think: Using U-Pb calcite geochronology to better constrain basin-bounding fault reactivation, Inner Moray Firth Basin, W North Sea. *Journal of the Geological Society* https://doi.org/10.1144/jgs2022-166

Tamas, A., Holdsworth, R.E., Underhill, J.R., Tamas, D.M., Dempsey, E.D., McCarthy, D.J., McCaffrey, K.J.W., & Selby, D., 2022. Correlating deformation events onshore and offshore in superimposed rift basins: The Lossiemouth Fault Zone, Inner Moray Firth Basin, Scotland. *Basin Research*, 34 (4), pp. 1314-1340. https://doi.org/10.1111/bre.12661

Tanner, P.W.G., 2008. Tectonic significance of the Highland Boundary Fault, Scotland.

Journal of the Geological Society London, 165, 915–921. https://doi.org/10.1144/0016-76492008-012

Tanner, P.W.G. 2014. A kinematic model for the Grampian Orogeny, Scotland. *Geological Society London, Special Publications,* 390, 467–511. https://doi.org/10.1144/SP390.23

Tanner, P.W.G., Armstrong, H.A. & Owen, A.W., 2013c. Rare earth element and La – Th – Sc analysis of cherts from the Highland Border Complex , Scotland: Geochemical determination of the sedimentary environment in greenschist facies rocks. *Scottish Journal of Geology*, 49, 15–31. https://doi.org/10.1144/sjg2012-464

Tanner, P.G., Bendall, C.A., Pickett, E.A., Roberts, J.L., Treagus, J.E. & Stephenson, D. 2013a. The Dalradian rocks of the south-west Grampian Highlands of Scotland. *Proceedings of the Geologists' Association*, 124, 83–147. https://doi.org/10.1016/j.pgeola.2012.07.008

Tanner, P.W.G & Sutherland, S., 2007. The Highland Border Complex, Scotland: a paradox resolved. *Journal of the Geological Society London*, 164, 111–116. https://doi.org/10.1144/0016-76492005-188

Tanner, P.G., Thomas, C.W., Harris, A.L., Gould, D., Harte, B., Treagus, J.E., Stephenson, D. 2013b. The Dalradian rocks of the Highland Border region of Scotland. *Proceedings of the Geologists' Association*, 124, 215–262. https://doi.org/10.1016/j.pgeola.2012.07.013

Tembe, S., Lockner, D.A. & Wong, T.F., 2010. Effect of clay content and mineralogy on frictional sliding behavior of simulated gouges: Binary and ternary mixtures of quartz, illite, and montmorillonite. *Journal of Geophysical Research: Solid Earth*, 115, 1–22. https://doi.org/10.1029/2009JB006383

Torgersen, E., Viola, G., Zwingmann, H. & Henderson, I.H.C., 2015. Inclined K–Ar illite age spectra in brittle fault-gouges: Effects of fault reactivation and wall-rock contamination. *Terra Nova*, 27, 106–113. https://doi.org/10.1111/ter.12136

Underhill, J.R., Monaghan, A.A. and Browne, M.A.E. 2008. Controls on structural styles, basin development and petroleum prospectivity in the Midland Valley of Scotland. Journal of Marine and Petroleum Geology, 25, 1000-1022.

Uysal, I.T., Delle Piane, C., James Todd, A. & Zwingmann, H., 2020. Precambrian faulting episodes and insights into the tectonothermal history of north Australia: Microstructural evidence and K–Ar , 40Ar–39Ar, and Rb–Sr dating of syntectonic illite from the intracratonic Millungera Basin. *Solid Earth*, 11, 1653–1679. https://doi.org/10.5194/se-11-1653-2020

Uysal, I.T., Mutlu, H., Altunel, E., Karabacak, V. & Golding, S.D., 2006. Clay mineralogical and isotopic (K–Ar , δ18O, δD) constraints on the evolution of the North Anatolian Fault Zone, Turkey. *Earth and Planetary Science Letters*, 243, 181–194. https://doi.org/10.1016/j.epsl.2005.12.025

Van Der Pluijm, B.A., Hall, C.M., Vrolijk, P.J., Pevear, D.R. & Covey, M.C., 2001. The dating of shallow faults in the earth's crust. *Nature*, 412, 172–175. https://doi.org/10.1038/35084053

Van Der Pluijm, B.A., Ho, N-C., Peacor, D.R. & Merriman, R.J., 1998. Contradictions of slate formation resolved? Nature, 392, 348. https://doi.org/10.1038/32810

Velde, B., 1965. Experimental determination of muscovite polymorph stabilities. *American Mineralogist*, 50, 436–449.

Verma, A.R. & Krishna, P., 1966. *Polymorphism and Polytypism in Crystals*. John Wiley and Sons.

Viola, G., Scheiber, T., Fredin, O., Zwingmann, H., Margreth, A. & Knies, J., 2016. Deconvoluting complex structural histories archived in brittle fault zones. *Nature Communications*, 7, 1–10. https://doi.org/10.1038/ncomms13448

Viola, G., Zwingmann, H., Mattila, J. & Käpyaho, A., 2013. K–Ar illite age constraints on the Proterozoic formation and reactivation history of a brittle fault in Fennoscandia. *Terra Nova*, 25, 236–244. https://doi.org/10.1111/ter.12031

Vrolijk, P., Pevear, D., Covey, M. & LaRiviere, A., 2018. Fault-gouge dating: history and evolution. *Clay Minerals*, 53, 305–324. https://doi.org/10.1180/clm.2018.22

Zwingmann, H. & Mancktelow, N., 2004. Timing of Alpine fault-gouges. *Earth and Planetary Science Letters,* 223, 415–425. https://doi.org/10.1016/j.epsl.2004.04.041

Zwingmann, H., Mancktelow, N., Antognini, M. & Lucchini, R., 2010. Dating of shallow faults: New constraints from the AlpTransit tunnel site (Switzerland). *Geology*, 38, 487–490. https://doi.org/10.1130/G30785.1

Figure 1. *The Highland Boundary Fault looking southwest across Craigeven Bay, Stonehaven.*

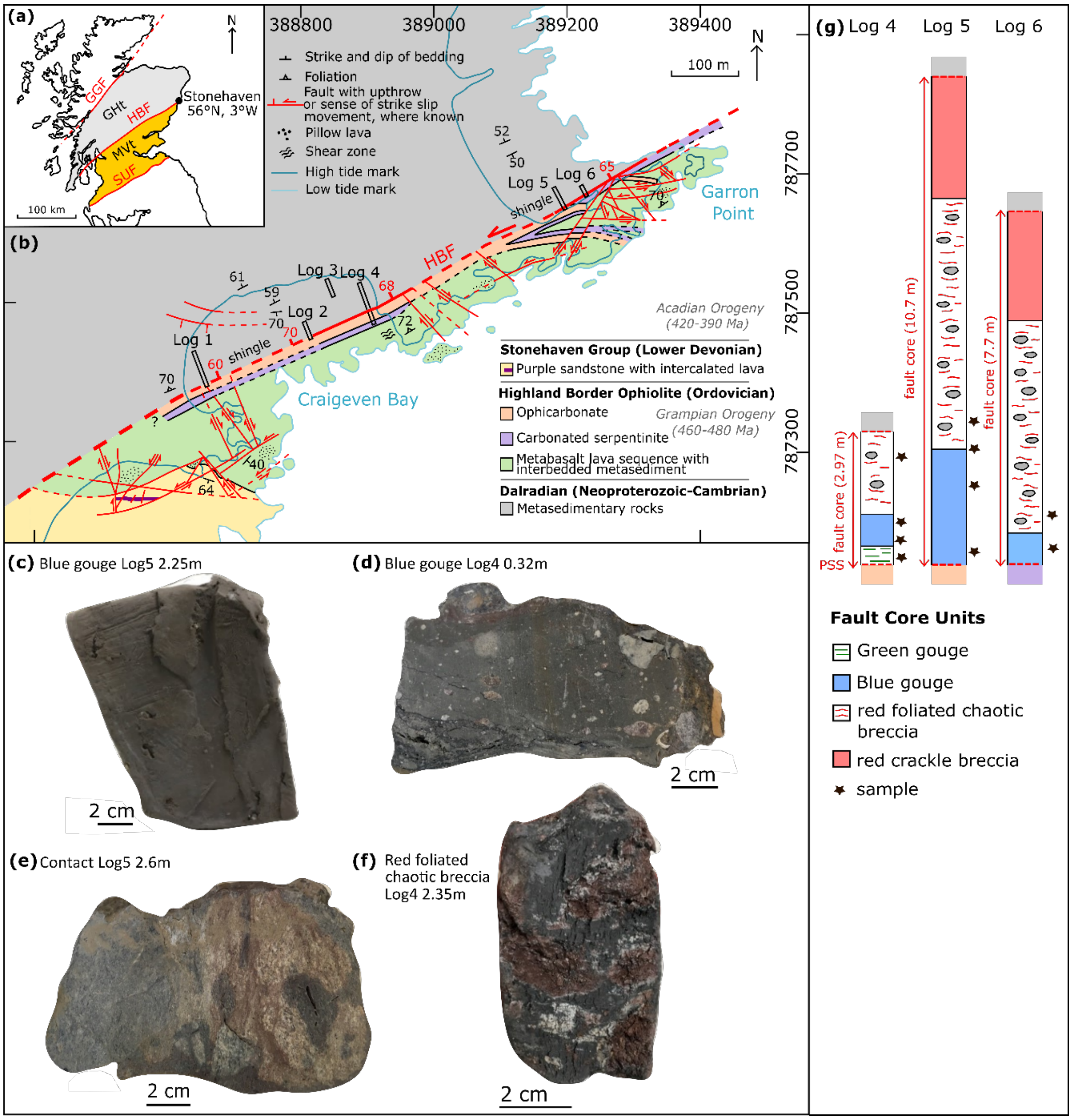

Figure 2. *The Highland Boundary Fault. a) Simplified geological map of Scotland showing the study site (GGF, Great Glen Fault; SUF; Southern Uplands Fault; GHt, Grampian Highlands terrane; MVt, Midland Valley terrane). b) Geological map of the Highland Boundary Fault from McKay et al. (2020). The location of measured structural logs is indicated by the black rectangles. c) Hand specimen of the blue gouge from Log 5, 2.25 m from the PSS. d) Hand specimen of the blue gouge from Log 4, 0.32 m from the PSS. e) Hand specimen of the contact between the blue gouge and red foliated chaotic breccia from Log 5, 2.6 m from the PSS. f) Hand specimen of the red foliated chaotic breccia from Log 4, 2.35 m from the PSS. g) Selected structural logs showing the internal structure and fault core units of the Highland Boundary Fault, sample locations in these sections are indicated by the black stars adjacent.*

968

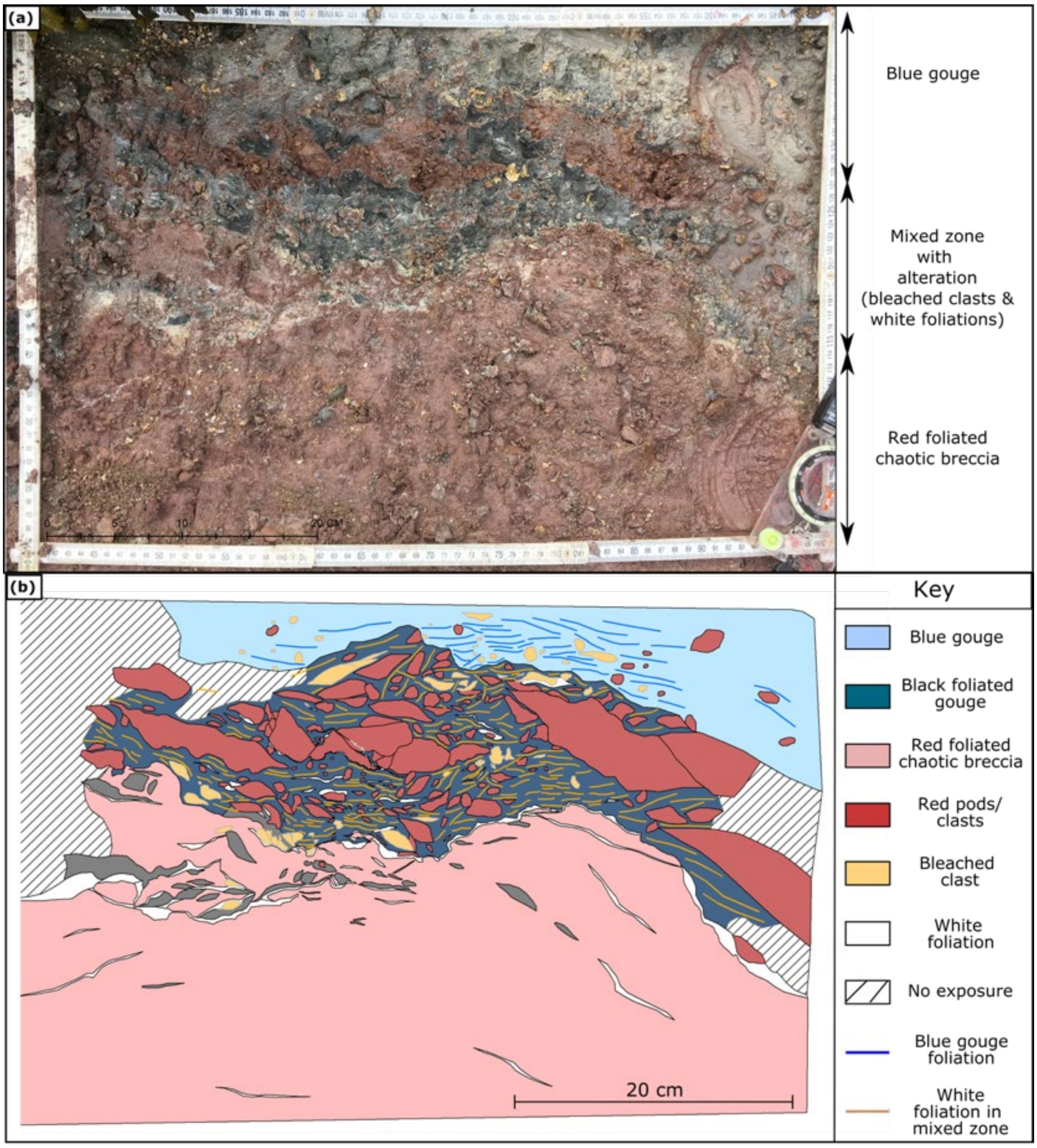

Figure 3. *Contact between the blue gouge and red foliated chaotic breccia at Log5-2.6m* ***(a)*** *Field photograph orientated sub-parallel to the HBF (orientation of ruler at strike 062°).* ***(b)*** *Digitised field photograph.*

969

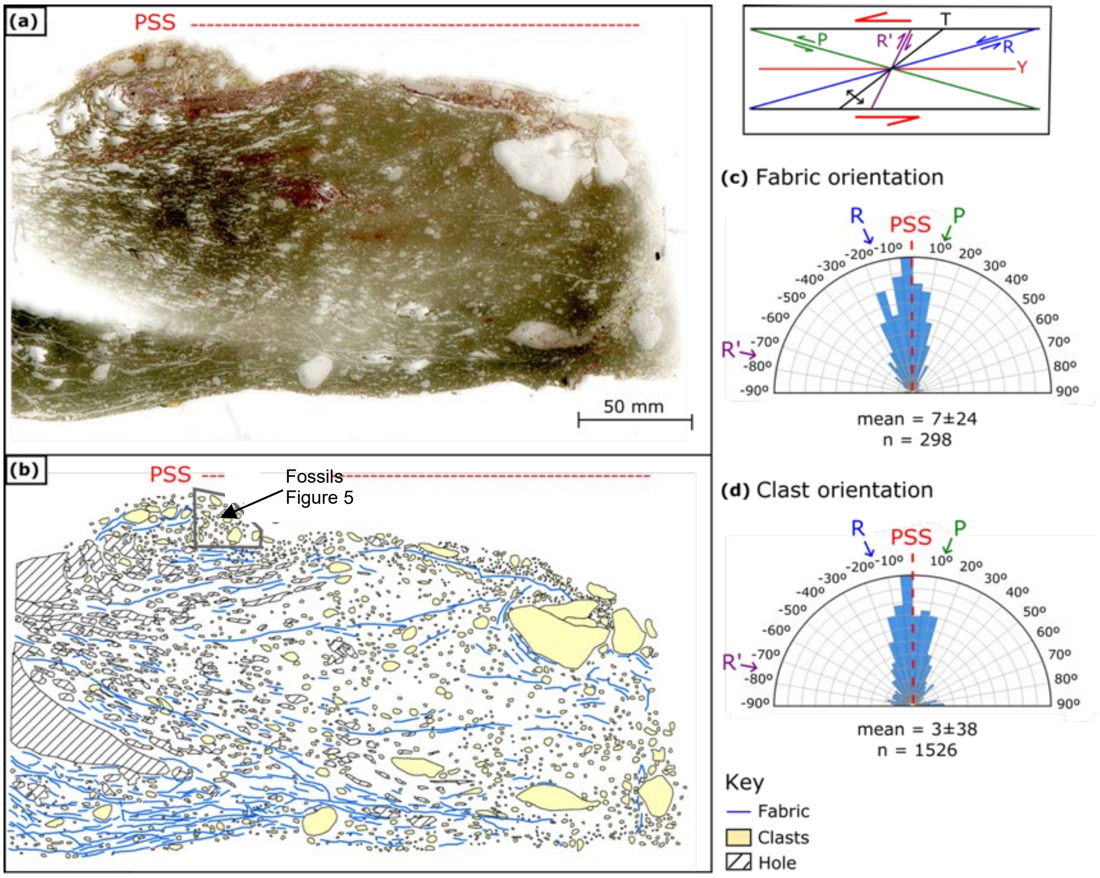

Figure 4. *Thin section of blue gouge (Log 4-0.32m).* ***(a)*** *Scanned thin section photo.* ***(b)*** *Digitised thin section.* ***(c)*** *Rose diagram of the orientation of the fabric with respect to the PSS of the HBF at 0°. The ± refers to standard deviation.* ***(d)*** *Rose diagram of the orientation of the long axis of the clasts with respect to the PSS of the HBF at 0º. (inset) Geometric features of an idealised Reidel shear zone in a sinistral strike-slip regime. Rose diagrams were created using GeoRose software.*

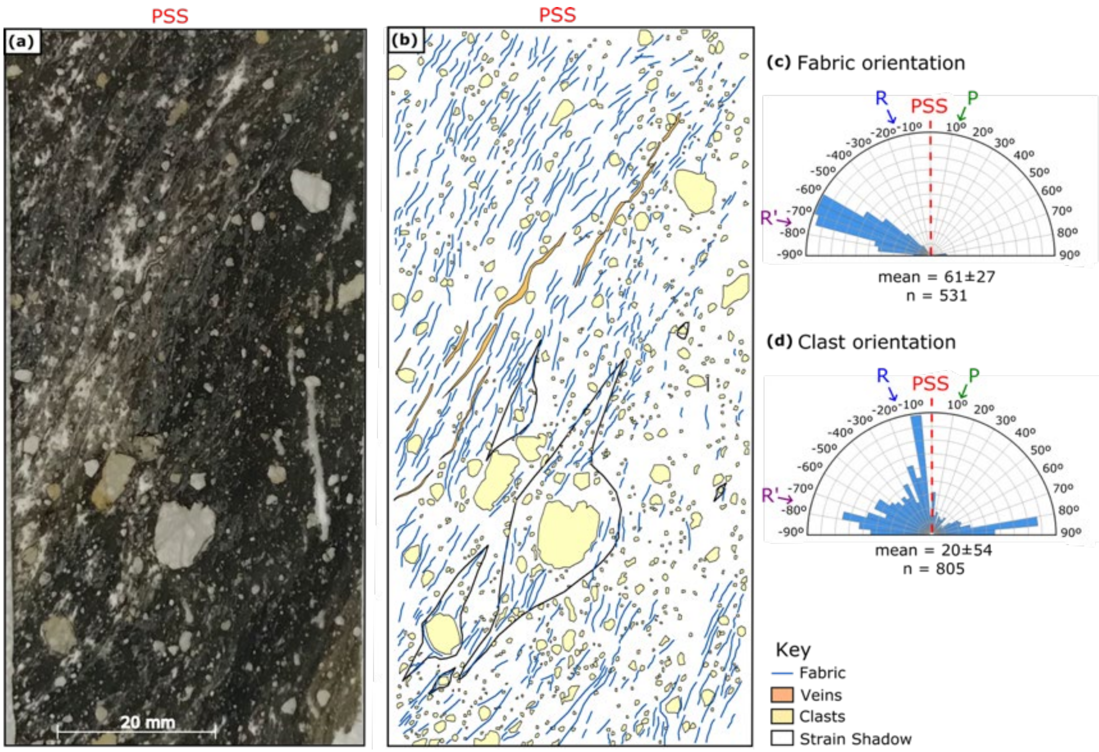

Figure 5. *Thin section of blue gouge (Log 5-2.25m).* ***(a)*** *Scanned thin section photo.* ***(b)*** *Digitised thin section.* ***(c)*** *Rose diagram of the orientation of the fabric with respect to the PSS of the HBF at 0°. The ± refers to standard deviation.* ***(d)*** *Rose diagram of the orientation of the long axis of the clasts with respect to the PSS of the HBF at 0º. Rose diagrams were created using GeoRose software.*

971

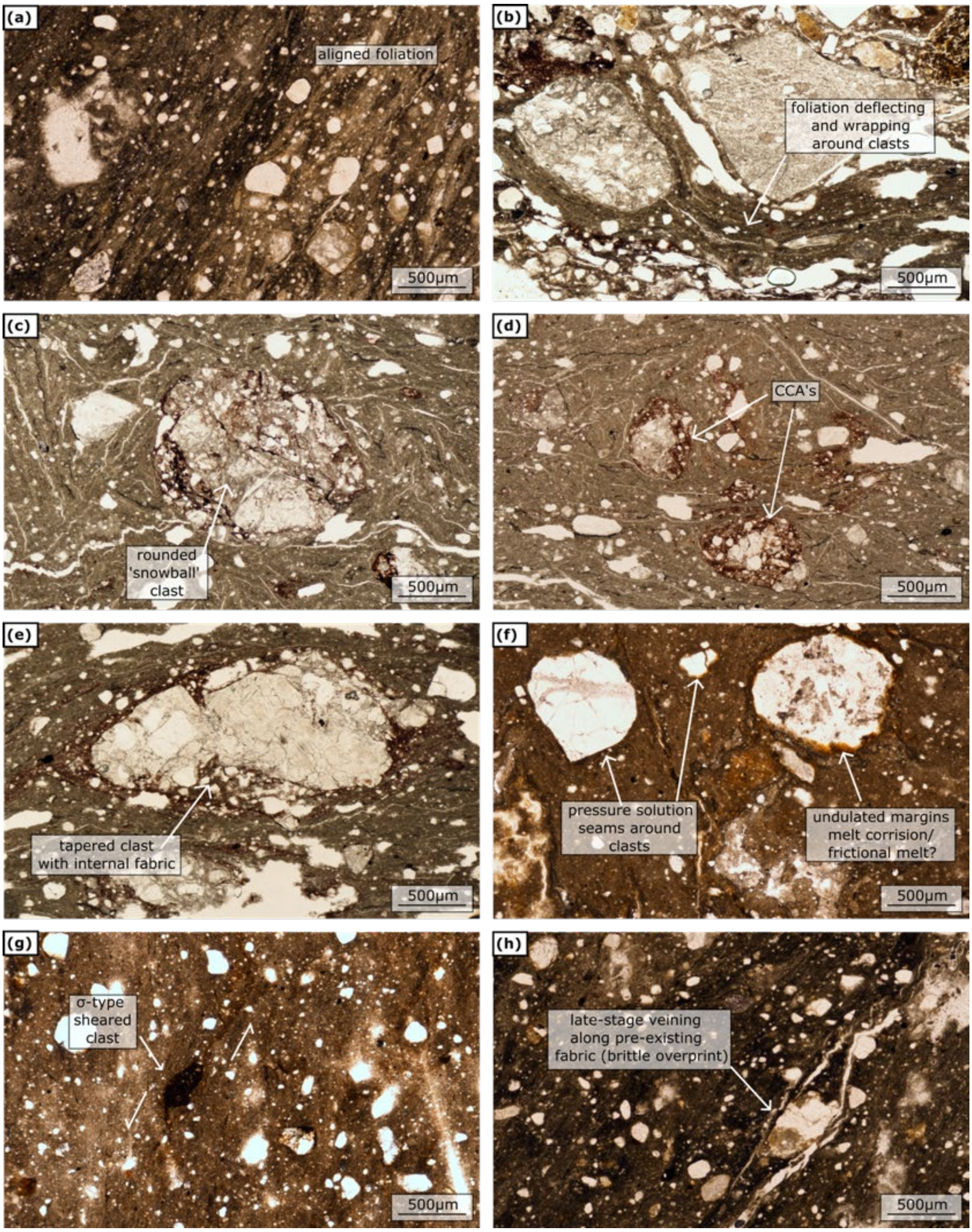

Figure 6. *Photomicrographs of the blue fault-gouge.* ***(a)*** *Aligned steeply dipping (60-75° from the PSS of the HBF) fabric in sample Log 5-2.25m.* ***(b)*** *Fabric deflecting and wrapping around clasts in sample Log 4-0.32m.* ***(c)*** *Rounded 'snowball' clast in sample Log 4-0.32m.* ***(d)*** *Clay clast aggregates (CCA's) in sample Log 4-0.32m.* ***(e)*** *Tapered clast with dissolution-precipitation seams around the edges in sample Log 4-0.32m.* ***(f)*** *Clasts with pressure solutions seams and undulated margins indicative of melt corrosion/frictional melt in sample Log 5-0.3m.* ***(g)*** *σ -type strain shadow showing evidence of shear strain in sample Log 5-0.3m.* ***(h)*** *Late-stage veining along a pre-existing fabric in sample Log 5-2.25m. All images in plane polarised light.*

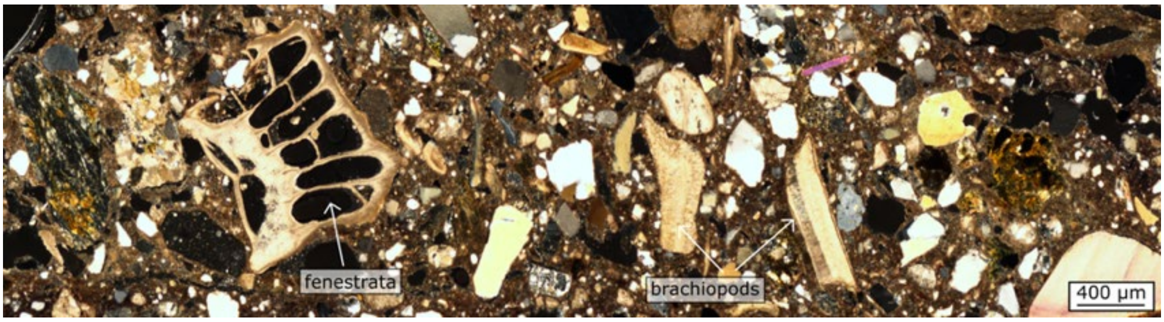

Figure 7. *Localised section of microfossils within the blue gouge (Log 4-0.32m; see* ***Figure 2*** *for location). This thin section is not orientated with respect to the PSS of the HBF. Image in plane polarised light.*

973

974

975

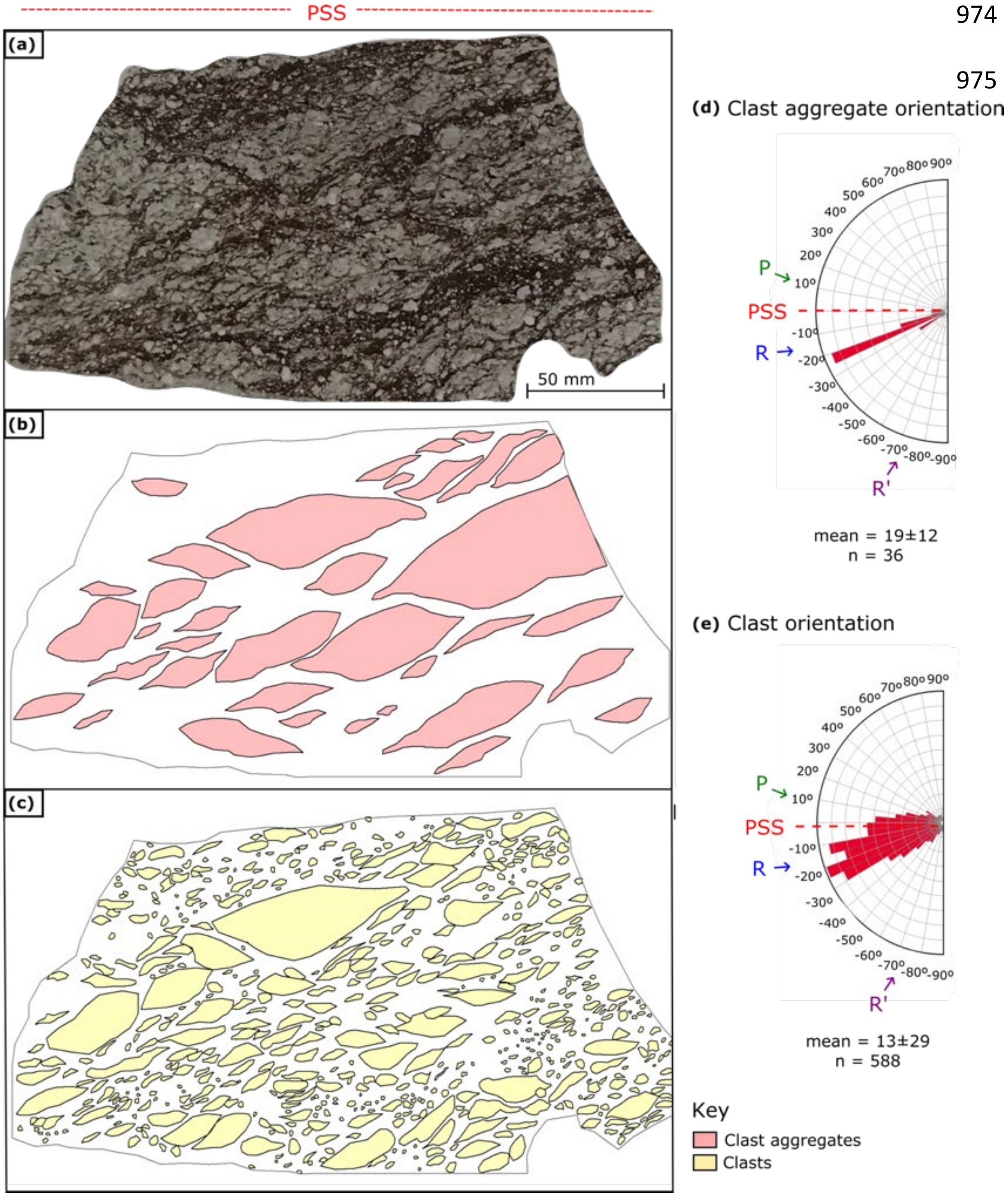

Figure 8. *Thin section of red foliated chaotic breccia (Log 6-1m).* ***(a)*** *Scanned thin section photo.* ***(b)*** *Digitised thin section showing aggregates of clasts.* ***(c)*** *Digitised thin section showing individual clasts.* ***(d)*** *Rose diagram showing the orientation of the long axis of the clast aggregates with respect to the PSS of the HBF at 0°. The ± refers to standard deviation.* ***(e)*** *Rose diagram showing the orientation of the long axis of the clasts with respect to the PSS of the HBF at 0º. Rose diagrams were created using GeoRose software.*

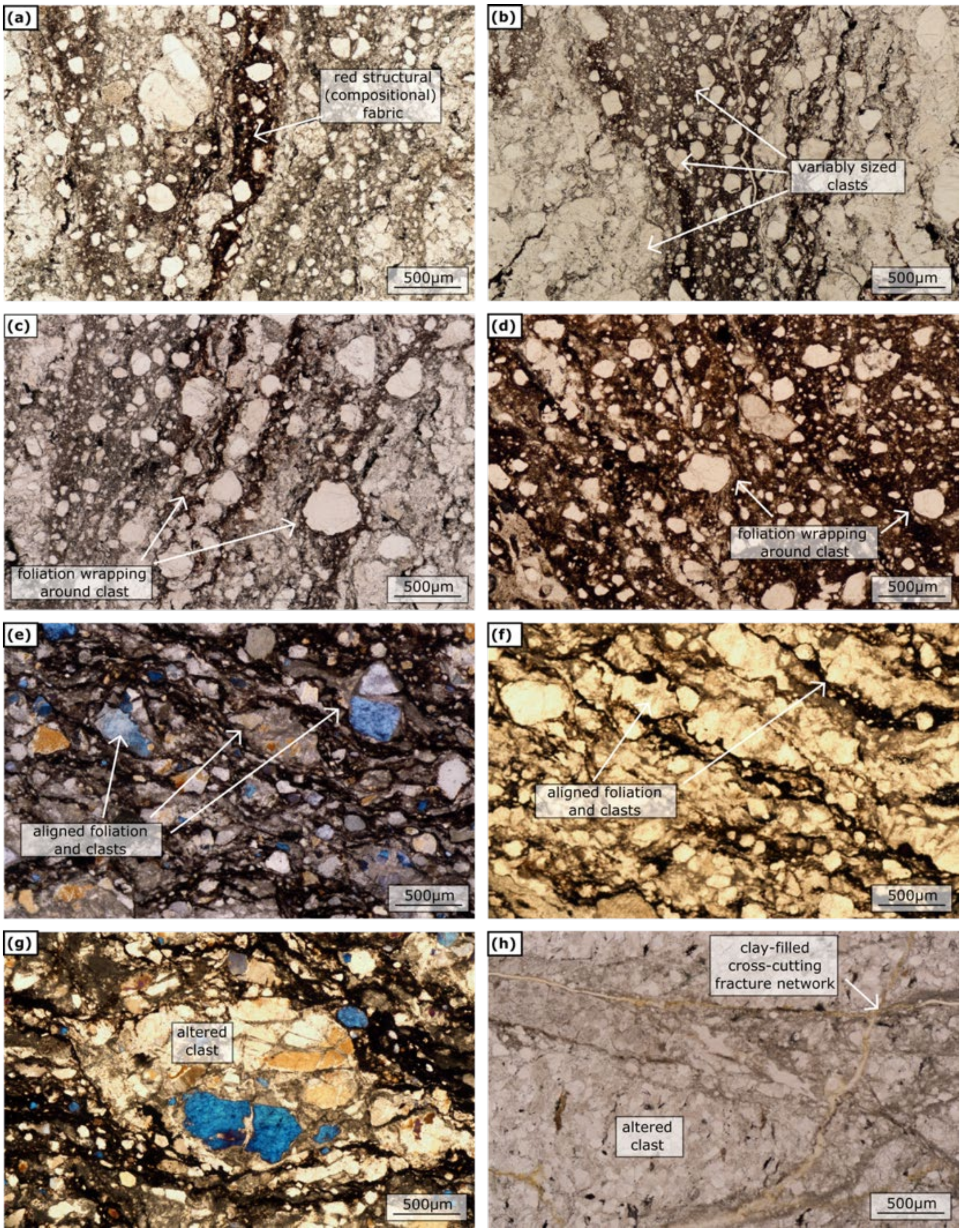

Figure 9. *Photomicrographs of the red foliated chaotic breccia all aligned in the same relative orientation to the HBF.* ***(a)*** *Evidence of red structural fabric in sample Log 4-2.35m.* ***(b)*** *Evidence of variable sized clasts in sample Log 4-2.35m.* ***(c)*** *Fabric deflecting and wrapping around clasts in sample Log 4-2.35m.* ***(d)*** *Fabric deflecting and wrapping around clasts in sample Log 5-2.9m.* ***(e)*** *Aligned foliation and clasts in sample Log6-1m.* ***(f)*** *Aligned foliation and clasts in sample Log 6-1m.* ***(g)*** *Altered clast in sample Log 6-1m. (h) Altered clast displaying an internal fabric and evidence of late-stage clay-filled fracture network in sample Log 4-2.35m. Images a-d, e and f are in plane polarised light. Images e and g are in cross-polarised light.*

976

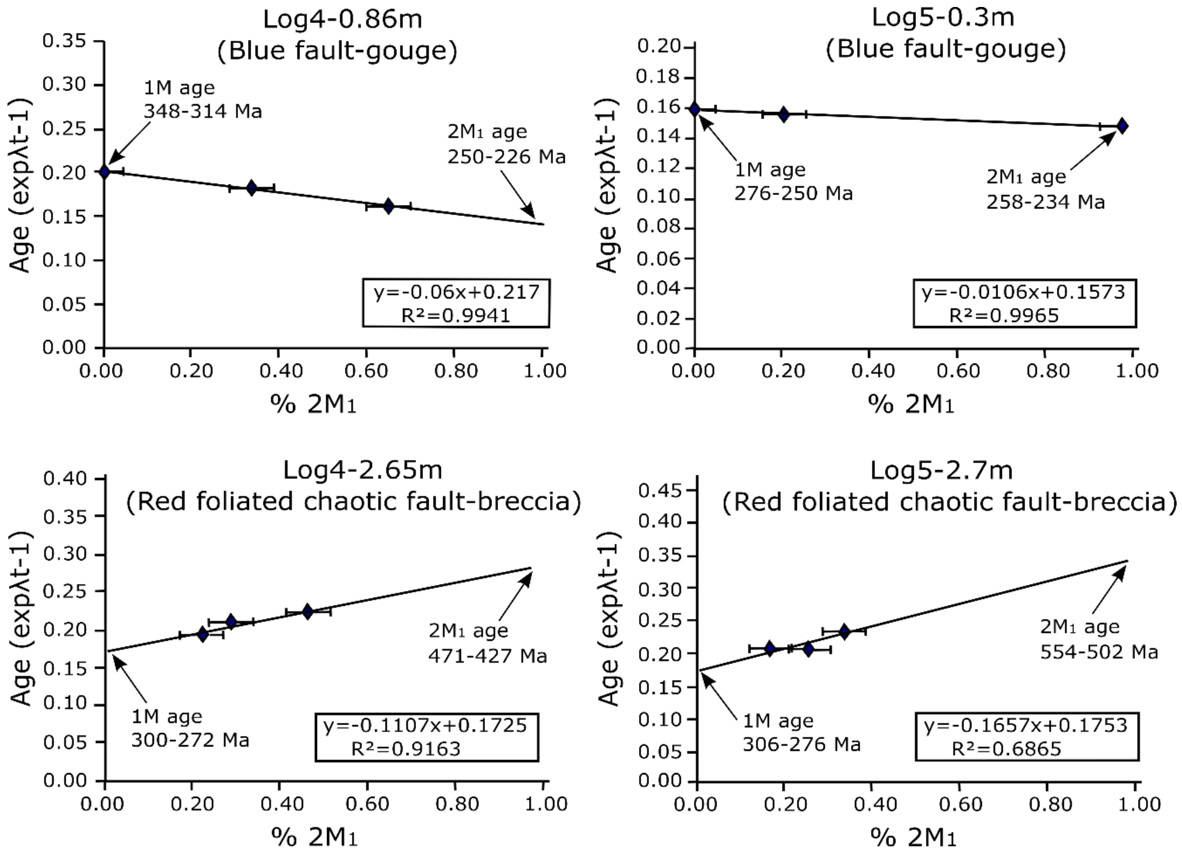

Figure 10. *Illite Age Analysis Plots (IAAP) for the four Highland Boundary Fault samples. Fraction error bars and end-member ages reflect ±5% error in quantification of %2M$_1$ illite polytype. Propagated errors for end-member ages are shown in labels only.*

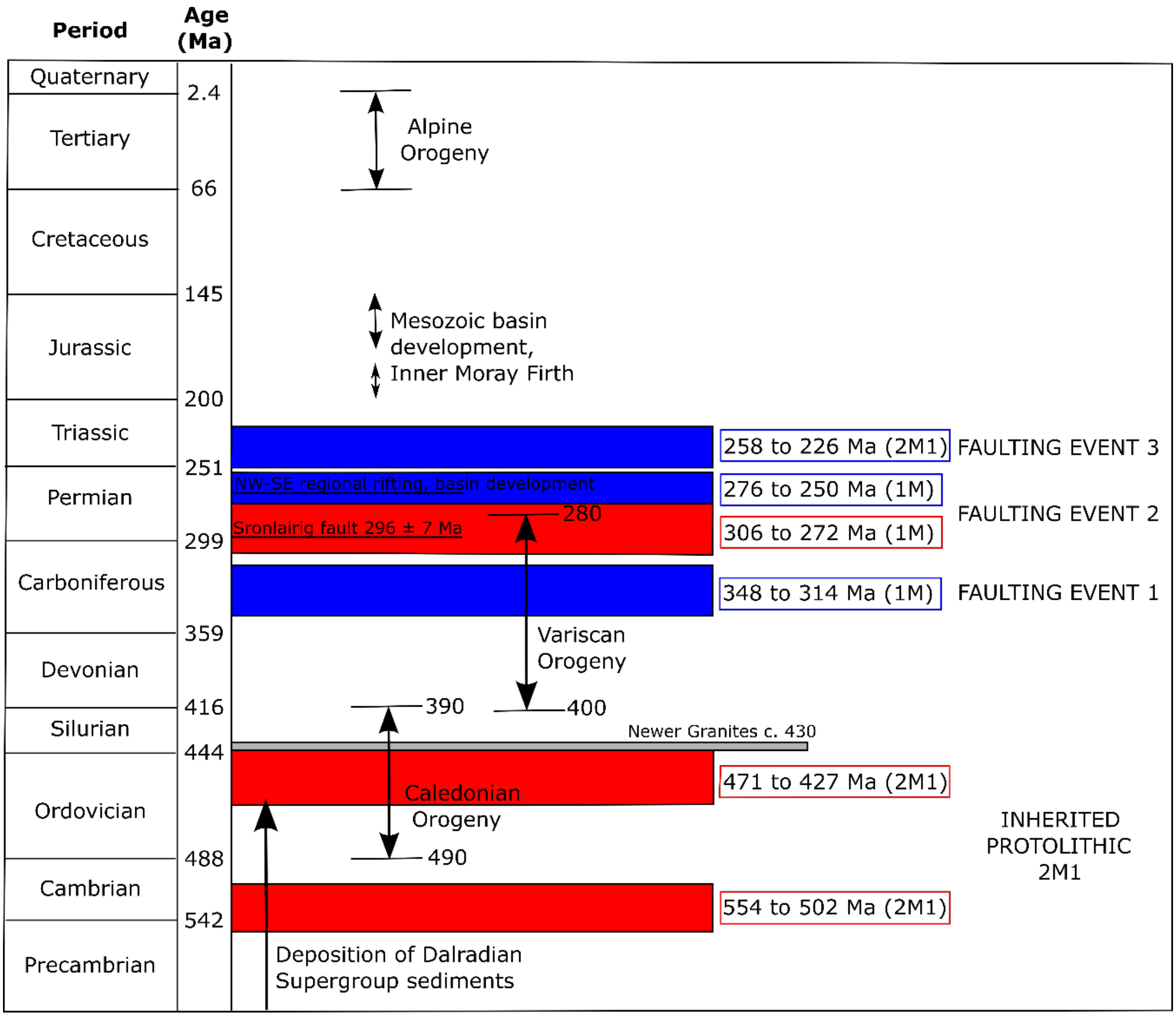

Figure 11. *Summary of faulting events related to the Highland Boundary Fault. Modified from Kemp et al. (2019). Simplified timescale from Gradstein et al. (2004). The red and blue bars indicate dates obtained from the red foliated chaotic fault-breccia and blue fault-gouge samples respectively.*

978

Standard	K (%)	Rad. ^{40}Ar (mol/g)	Rad. ^{40}Ar (%)	Age (Ma)	Error (Ma)	Error to reference (%)
HD-BP-155	7.96	3.361E-10	91.19	24.19	1.33	-0.08
LP6-169	8.37	1.917E-09	92.27	127.44	1.66	-0.36

Table 1. *K–Ar standards data. Standard error to reference HD-B1 (Hess and Lippolt, 1994) and LP6 (Odin et al. 1982).*

Airshot data	$^{40}Ar/^{36}Ar$	±
AS148-AirS-2	295.74	0.22

Table 2. *Airshot data.*

			Relative % of minerals								
Sample	**Fault core unit**	**% clay ***	**Illite**	**Chl**	**Kaol**	**Qtz**	**Hal**	**Hem**	**Rut**	**Calc**	**Ana**
Log4 0.86m 1–0.5µm		78	24	12	42	17	nd	2	1	nd	2
Log4 0.86m 0.5–0.2µm	BG	95	39	29	27	3	1	nd	nd	nd	1
Log4 0.86m <0.2 µm		89	64	17	8	3	7	nd	nd	nd	nd
Log5 0.3m 1–0.5µm		81	13	48	20	14	nd	1	1	nd	3
Log5 0.3m 0.5–0.2µm	BG	98	9	68	19	2	2	nd	nd	nd	2
Log5 0.3m <0.2 µm		94	26	55	13	2	2	nd	nd	nd	2
Log4 2.65m 1–0.5µm		89	64	nd	25	7	nd	4	nd	nd	nd
Log4 2.65m 0.5–0.2µm	RFCB	100	87	nd	10	3	nd	nd	nd	nd	nd
Log4 2.65m <0.2 µm		92	89	nd	3	2	6	nd	nd	nd	nd
Log5 2.7m 1–0.5µm		75	56	nd	19	11	nd	13	nd	nd	1
Log5 2.7m 0.5–0.2µm	RFCB	94	82	nd	10	2	nd	6	nd	nd	nd
Log5 2.7m <0.2 µm		71	66	nd	5	2	17	nd	nd	10	nd

∗ Clay proportions are further explained in **Table 4**.

***Table 3**. XRD results of the bulk mineralogical composition (wt.%) of the recovered size fractions. Chl, Chlorite; Kaol, Kaolinite; Qtz, Quartz; Hal, Halite; Hem, Hematite; Rut, Rutile; Calc, Calcite; Anat, Anatase; nd, not detected; BG, Blue fault-gouge; RFCB, Red foliated chaotic fault-breccia. Refer to the Supplementary Information for the annotated XRD traces.*

		Relative % of clay minerals				Illite polytypes	
Sample	**Fault core unit**	**Chlorite (Tri)**	**Kaolinite**	**I+I/S**	**% Exp**	**Relative % of $1M_d$**	**Relative % of $2M_1$**
Log4 0.86m 1–0.5µm	BG	16	32	52	15	100	0
Log4 0.86m 0.5–0.2µm		na	na	na	na	66	34
Log4 0.86m <0.2 µm		13	4	83	15	35	65
Log5 0.3m 1–0.5µm	BG	54	12	34	15	100	0
Log5 0.3m 0.5–0.2µm		na	na	na	na	79	21
Log5 0.3m <0.2 µm		42	2	56	15	0	100
Log4 2.65m 1–0.5µm	RFCB	0	12	88	15	53	47
Log4 2.65m 0.5–0.2µm		na	na	na	na	71	29
Log4 2.65m <0.2 µm		0	2	98	15	78	22
Log5 2.7m 1–0.5µm	RFCB	0	10	90	15	66	34
Log5 2.7m 0.5–0.2µm		na	na	na	na	83	17
Log5 2.7m <0.2 µm		0	4	96	15	74	26

Table 4. *XRD results showing the relative percentages of clay minerals in the various clay fractions as determined from oriented specimens. Chlorite (Tri), Trioctahedral Chlorite; I+I/S= Illite plus mixed-layer illite/smectite; % Exp, expandability of mixed-layer illite/smectite; na= not available. Illite polytypes obtained by full pattern fitting of $1M_d$ and $2M_1$ illite standards. BG, Blue fault-gouge; RFCB, Red foliated chaotic fault-breccia. Refer to the Supplementary Information for the annotated XRD traces.*

Sample	Size Fraction	Fault core unit	K (%)	Rad. ^{40}Ar (mol/g)	Rad. ^{40}Ar (%)	Age (Ma)	Error (Ma)
Log4 0.86m	1–0.5µm	BG	2.10	1.317E-09	96.7	329.4	7.6
	0.5–0.2µm	BG	3.87	2.111E-09	96.5	302.5	7.0
	<0.2µm	BG	5.11	2.580E-09	94.5	269.9	6.2
Log5 0.3m	1–0.5µm	BG	1.74	8.556E-10	94.2	263.3	6.1
	0.5–0.2µm	BG	2.42	1.168E-09	93.7	258.9	6.0
	<0.2µm	BG	3.67	1.681E-09	92.7	246.5	5.7
Log4 2.65m	1–0.5µm	RFCB	4.97	3.471E-09	98.7	363.4	8.4
	1–0.5µm (duplicate)	RFCB	4.97	3.451E-11	98.4	361.6	8.3
	0.5–0.2µm	RFCB	5.67	3.703E-09	98.0	341.9	7.9
	0.5–0.2µm (duplicate)	RFCB	5.67	3.708E-09	98.2	342.4	7.9
	<0.2µm	RFCB	5.94	3.575E-09	96.2	317.4	7.3
	<0.2 (duplicate)	RFCB	5.94	3.594E-09	96.6	318.9	8.2
Log 5 2.7m	1–0.5µm	RFCB	4.22	3.127E-09	98.7	383.4	8.8
	0.5–0.2µm	RFCB	4.84	3.151E-09	97.1	341.0	7.9
	<0.2µm	RFCB	4.66	3.016E-09	97.6	339.2	7.9

Table 5*. K–Ar analyses of the blue fault-gouge (BG) and red foliated chaotic fault-breccia (RFCB). The duplicates are separate splits from each fraction.*